Space Weather

RESEARCH ARTICLE
10.1029/2024SW003938

Response of the Thermosphere-Ionosphere System to an X-Class Solar Flare: 30 March 2022 Case Study

Volkan Sarp[1], Erdal Yiğit[2,3], and Ali Kilcik[1]

[1]Department of Space Science and Technologies, Akdeniz University, Antalya, Türkiye, [2]Department of Physics and Astronomy, Space Weather Lab, George Mason University, Fairfax, VA, USA, [3]Goddard Space Flight Center, NASA, Greenbelt, MD, USA

Key Points:

- Spectral content and temporal variation of total electron content perturbations associated with an X1.3 Solar Flare are analyzed
- The thermosphere-ionosphere exhibits a longitudinal flare response during the recovery phase
- The nonlinear interaction of the solar flare with the southward turning of the interplanetary magnetic field B_z introduces significant variability

Correspondence to:
V. Sarp and E. Yiğit,
theneutron@gmail.com;
eyigit@gmu.edu

Citation:
Sarp, V., Yiğit, E., & Kilcik, A. (2024). Response of the thermosphere-ionosphere system to an X-class solar flare: 30 March 2022 case study. *Space Weather*, *22*, e2024SW003938. https://doi.org/10.1029/2024SW003938

Received 28 MAR 2024
Accepted 16 SEP 2024

Abstract The response of the thermosphere ionosphere system to an X1.3 class solar flare is studied using observations of the total electron content (TEC) and the Global Ionosphere Thermosphere Model (GITM) simulations. The solar flare erupted from the active region AR12975 on 30 March 2022. Owing to the absence of accompanying severe geomagnetic activity, it was possible to isolate the effects of the flare on the upper atmosphere. TEC data are processed for Continental USA (CONUS), employing filtering and binning techniques to create 2D variation maps. The spectral content of the TEC variations is analyzed using a wavelet coherence method. The immediate response of the solar flare exhibited broad similarities, while notable differences were observed during the recovery period between the East and West sides of the CONUS. GITM is used to explore the East–West asymmetry of the key T-I parameters. Simulation results reveal that the coinciding interplanetary magnetic field southward turning had a greater influence on these parameters compared to the solar flare, while their nonlinear interaction introduced complex variations. Additional investigation reveals gravity wave damping also contributes to the asymmetric solar flare response.

Plain Language Summary This study examines how a solar flare, which erupted on 30 March 2022, affected the Earth's upper atmosphere. We used satellite data to measure changes in the amount of charged particles in the atmosphere above the United States (specifically the area known as CONUS) and ran computer simulations to better understand these changes. We found that while the immediate reaction of the atmosphere to the flare was similar across the CONUS, differences emerged between the East and West during the recovery phase. The simulations showed that these differences were influenced by local time differences between the East and West, as well as by variations in the Earth's magnetic field geometry above these regions. Additionally, the study identified that the damping of gravity waves also played a role in these regional differences. Overall, the research highlights how complex interactions between various factors can lead to different responses to solar events in different parts of the CONUS.

1. Introduction

The thermosphere is the uppermost layer of Earth's atmosphere characterized by extreme temperature variations and a high degree of ionization associated with lower atmospheric and space weather processes (Koucká Knížová et al., 2021; Shiokawa & Georgieva, 2021; Ward et al., 2021; Yiğit, Koucká Knížová, et al., 2016). The ionosphere is a naturally occurring plasma environment in the upper atmosphere, composed of ions and free electrons, coexisting with neutral particles. The thermosphere-ionosphere (T-I) system represents a synergistic interplay between the electrically charged region of the ionosphere and the neutral thermosphere, highlighting the essential need for a comprehensive systems approach to understand their complex interactions.

Solar flares are intense bursts of energy and radiation from the Sun, creating a much larger variation than typical background variability. The sudden enhancement of X-ray and extreme ultraviolet (EUV) irradiance during a solar flare introduces excessive ionization of the neutral components, creating transient variations in the composition, temperature, dynamics, and electrodynamics of the T-I system (J. Liu et al., 2021; Mitra, 1974; Sutton et al., 2006; R. Zhang et al., 2017). Flare impacts on a global scale vary depending on flare characteristics (Le et al., 2013; J. Y. Liu et al., 2006), flare location on the solar disk (Qian et al., 2010), and the state of the T-I region during the flare event (Qian et al., 2020). H. Liu et al. (2007) suggested that flare-induced neutral and plasma disturbances are de-coupled during the first few hours following the flare onset.

The T-I system exhibits significant longitudinal variations. The variations in the thermosphere arise from the superposition of non-migrating diurnal tides, particularly terdiurnal and 6-hr tides, which originate in the lower atmosphere and propagate into the T-I system (Lilienthal et al., 2020; Miyoshi, 2021). The longitudinal variability of the ionosphere is clearly demonstrated by the East–West asymmetry observed in Total Electron Content (TEC) data over the Continental USA (CONUS) (S.-R. Zhang et al., 2011) and in electron density data over the Far East Region (Zhao et al., 2013). The longitudinal dependence of ionospheric dynamics is linked to localized sources such as gravity waves and neutral winds (Yizengaw, 2021).

The longitudinal variability influences the solar flare response of the T-I system. On a local scale, flare impacts are observed in the equatorial electrojet strength, showing positive or negative changes at different longitudes during the same flare (Manju et al., 2009; Sripathi et al., 2013). Simulations of the T-I response to solar flares have demonstrated that the vertical expansion of the thermosphere depends on the solar zenith angle, which drives temperature and density disturbances (Pawlowski & Ridley, 2008). Since the solar zenith angle is longitude dependent, this adds another layer of complexity to the longitudinal variability. Moreover, simulations have reported strong localized enhancements of Joule heating during solar flares, resulting in increased vertical expansion of the thermosphere (Qian et al., 2012). These local increases in Joule heating can cause deviations from hydrostatic equilibrium, launching acoustic-gravity waves that reach F-region heights and introduce further disturbances in the T-I system (Smith, 1998).

Disturbances in the thermosphere play a pivotal role in satellite drag, which in turn affects satellite stability, orbital dynamics, and the risk of collisions with other objects, while disturbances in the ionosphere have significant implications for communication, navigation, and surveillance systems, as they can introduce temporary irregularities in electron density and disrupt the propagation of radio waves. Recent studies demonstrated the space weather effects of EUV and X-ray variations during modest solar flares (Belcher et al., 2021; Briand et al., 2021; C. Marqué, et al., 2018). Prior studies investigated the disturbances of ionosphere and thermosphere induced by large solar flares during accompanying geomagnetic storms (e.g., Li et al., 2018; X. Liu et al., 2022; S.-R. Zhang et al., 2019).

The goal of this paper is to investigate the response of the T-I system to an X1.3 solar flare that occurred on 30 March 2022, coninciding with the southward turning of the IMF B_z during a period of low geomagnetic activity. TEC products for a dense receiver network along the Continental United States (CONUS) are processed to analyze the ionospheric response. The Global Ionosphere Thermosphere Model (GITM) is used to study the response of the T-I system during the event. In Section 2, observations and data processing steps are explained, along with the set-up of GITM simulations using empirical Flare Irradiance Spectral Model (FISM). Results are presented and discussed in Section 3. Finally, conclusions and summary are given in Section 4.

2. Data and Methodology

2.1. Total Electron Content Data

Various techniques have been employed to monitor ionospheric solar flare effects. The agreement between theoretical predictions and observations of J. Y. Liu et al. (2004) demonstrated that the TEC monitoring is more suitable to study solar flare effects compared to most of the techniques which simply observe flare features at certain altitudes. TEC is a measure of the integrated number of free electrons along a trans-ionospheric signal path calculated by the propagation time difference between two different radio frequencies (Mannucci et al., 1998). TEC is expressed in TEC unit (TECu), corresponding to the total number of electrons contained in a column of cross-sectional area 1 m^2, extending upward from Earth's surface through the ionosphere. One TECu is defined as 1×10^{16} el/m^2.

Around 5,000 dual-frequency multi-channel ground-based receivers of the global navigation satellite system (GNSS) and multiple satellites operated by GPS/GLONASS are processed by MIT Haystack Observatory (Rideout & Coster, 2006; Vierinen et al., 2016) on a daily basis to produce line-of-sight (LOS) TEC data. LOS TEC, characterized by the elevation and azimuth of the measurement, refers to the one-dimensional line integral between any receiver-satellite pairing. This quantity, measured only along a limited number of paths and range of orientations, is insufficient to represent the complete structure and state of the ionosphere. Various approaches have been employed to produce two-, three-, and four-dimensional maps of electron density processing LOS TEC (Bust & Mitchell, 2008).

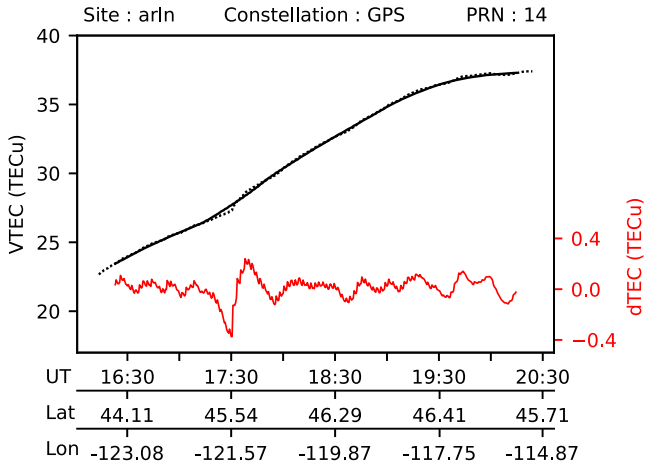

Figure 1. Demonstration of the data processing. Observed VTEC values for a specific site-satellite pair is shown by the dotted curve as a function of Universal Time. Bottom horizontal axes show the Latitude (Lat) and Longitude (Lon) coordinates of the ionospheric pierce point associated with the VTEC measurement at each time step. Solid curve represents the SG filtered version of the VTEC time-series. Difference between the observed and SG filtered VTEC time-series (dTEC, shown by the red curve) is used as the main data for further analysis.

With the fundamental assumption of the stationarity of the medium during the measurement, the slanted line integral measurement of electron density can be converted into an equivalent vertical line integral measurement called vertical TEC (VTEC). Each measurement can then be mapped to a spatial coordinate known as ionospheric pierce point (IPP). The IPP is defined as the intersection of the receiver-satellite ray with a reference altitude, which is typically based on the peak of a modeled electron density profile. Various methods of converting slant to vertical TEC are evaluated in Zhong et al. (2015).

VTEC data of each receiver-satellite pair can be considered as a time-series product. The bulk of time-series data within the spatial and temporal range of interest is suitable for time-series analysis methodology. Detrending is a crucial procedure for analyzing the temporal variations of TEC, as it can highlight deviations from the mean structure of TEC. Various filtering procedures used to detect wave signatures in TEC are evaluated in the work by Maletckii et al. (2020).

The Savitzky–Golay (SG) filter is a robust detrending method capable of detecting even small-scale TEC disturbances (Osei-Poku et al., 2021). The SG filter with a linear basis and a 30-min window has been applied to detect TEC disturbances triggered by solar eclipses (S.-R. Zhang et al., 2017), solar flares (S.-R. Zhang et al., 2019), and penetration electric fields (S.-R. Zhang et al., 2023). Considering the typical duration of the impulsive and flash phases of solar flares (Benz, 2016) and the temporal evolution of the studied solar flare (Figure 3a), we applied the same SG filter to detrend the VTEC data provided by MIT Haystack Observatory for 30 March 2022. Using the same methodology as prior studies allows for the comparison of our results with those studies.

Given the 0.5 min temporal resolution of VTEC data, the SG filter is applied with a 60-step window, corresponding to a constant 30-min temporal interval with varying spatial range for different GNSS site-satellite pairings. Ionospheric perturbations are evaluated by the detrended TEC (dTEC), which is the difference between the observed VTEC values and filtered VTEC values. A half-window length is excluded from both ends of each dTEC time series to prevent extrapolation-related spurious effects. A demonstration of the detrending procedure is given in Figure 1 for an arbitrary GNSS site located at 45.70° North and 120.18° West coordinates, locked to a GPS satellite whose pseudo range number is 14. During the recording, dTEC of up to ±0.35 TECu was observed.

Spatially scattered VTEC data can be organized (binned) and interpolated using image processing techniques to create 2D TEC maps. Numerous interpolation schemes for reconstructing TEC maps are evaluated in Foster and Evans (2008). For irregularly spaced data, the interpolation kernel must be sufficiently large to ensure that at least one input point is included at every output position. However, some resolution and magnitude may be lost due to an extended kernel. An alternative approach is to extend the spatial coverage of input points by binning the VTEC data, where each bin corresponds to a pixel. Pixel values are obtained by averaging all VTEC measurements whose IPP coordinates fall within the corresponding latitude and longitude intervals of the bin. The pixel (bin) size is the decisive factor in the resolution of 2D TEC maps. This binning technique has been previously employed to demonstrate the characteristics of mesoscale ionospheric irregularities (Nykiel et al., 2017; Tsugawa et al., 2007). On the other hand, Hernández-Pajares et al. (2017) emphasized the need for caution when using this approach to analyze wave-like disturbances, especially, if the interreceiver distances are less than half wavelength and/or the dense receiver network of the studied area spans less than two wavelengths.

Detrended TEC data is further processed into two-dimensional maps for the region spanning from 23°N to 55°N latitude and from 63°W to 131°W longitude, given the dense spatial coverage provided by GNSS receivers. This area essentially encompasses the continental United States, hereafter referred to as CONUS. TEC data with satellite elevation angles of less than 30° are excluded to reduce the uncertainty of location where the TEC is mapped. Cutoff time is taken as 45 min to exclude short or interrupted data. A site-satellite pairing that produced any rejected measurement is completely excluded during the corresponding signal. After applying these criteria, all remaining VTEC data for CONUS during the studied period are detrended into dTEC. Subsequently, a

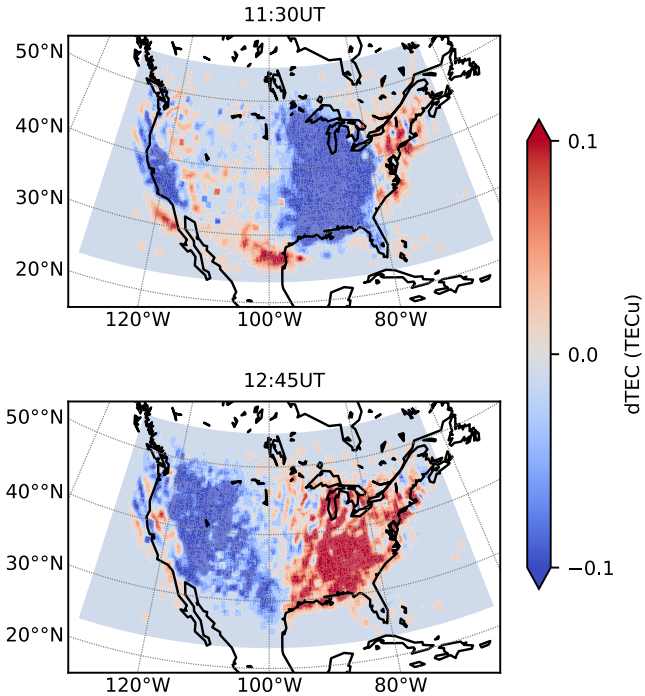

Figure 2. Examples of the processed data presented as specific instances of two-dimensional dTEC maps during the passage of the sunrise terminator. The maximum amplitude of the absolute dTEC is saturated at 0.1 for better visualization. In the upper panel, sunrise terminator effects are self-evident between 100°W and 80°W as negative dTEC values. The artificial effect of the SG filter, resulting in negative dTEC values backward in time, is explained in the text. The wave-fronts following the terminator passage are visible on the east side of the terminator. The lower panel displays the instance after 75 min, where the sunrise terminator effects have shifted 20° in longitude, and the following wave-fronts have become more pronounced.

magnitude cutoff of 3 TECu is applied to dTEC values to identify and reject corrupted data caused by errors or anomalies, such as cycle slips, in the phase measurements of the signal. The entire signal that produced corrupted data is also excluded.

The valid dTEC time series are then mapped into 2D dTEC maps with a pixel size determined as 0.15° × 0.15° in latitude and longitude. The value of a given pixel at a specific time instant is determined by averaging all dTEC values, whose IPP coordinates cross the spatial bin of that pixel at that specific time instant. The original temporal resolution (30-s) of the VTEC data is preserved. After populating all pixels with the respective averaged dTEC values across all time sequences, each pixel undergoes temporal smoothing through a 5-min running average. Subsequently, spatial interpolation is applied on each 2D dTEC map using a box filter with a kernel size 7 × 7 pixels, corresponding to a window size of 1.05° × 1.05° in latitude and longitude.

An arbitrary example of two dTEC maps during the passage of the sunrise terminator (ST) is illustrated in Figure 2. In the upper panel, the ST is revealed as negative variations spanning between 80°W and 100°W. It is important to note that the actual effect following an ST-passage results in a positive dTEC due to increasing ionization. However, the initial negative dTEC is an artifact caused by the width of the SG filter window, which captures past lower values as well as high values forward in time. Consequently, the TEC enhancement at a specific time will affect the filtered values backward in time due to the convolution of SG filter window in the temporal axis.

To be more specific, if we call the half-width of the SG filter window x, an increase in TEC values at time t starts enhancing the SG filtered values at time $t - x$. Thus, the dTEC at time $t - x$, calculated as the difference between the observed TEC and the enhanced SG filtered values, will provide artificial results, lasting until time $t + x$. The initial negative dTEC response after a solar flare caused by the artificial effect of SG filter is also mentioned in the work by S.-R. Zhang et al. (2019).

The lower panel of Figure 2 shows the ST at another instant, 75 min after the upper panel. The initial negative response shifted westward, and the subsequent positive response appeared instead. During this transition, some wavefronts are observed around 45° North latitude.

2.2. Analysis of Ionospheric Disturbances

Local frequency contents of the ionospheric disturbances are further analyzed by a generalized wavelet coherence as described in the work by Yang et al. (2023). Temporal variations of pixel values during the studied period are used as the input signals for the continuous wavelet transform (CWT). This method uses a window function ψ, known as the mother wavelet function. The temporal evolution of the frequency contents of the input signal can be determined by calculating the inner products of the input signal with scaled and time-shifted versions of the mother wavelet. The details of the wavelet analysis are presented in Appendix A.

2.3. Space Weather Conditions

Figure 3 shows the solar and geophysical indices between 09:00 UT and 23:45 UT on 30 March 2022. Panel a shows the integrated solar X-Ray flux at 0.1–0.8 nm measured by GOES-16. Panels b, c, and d show the interplanetary magnetic field (IMF) B_z vector, solar wind speed, and density, respectively, provided by NASA SPDF (King & Papitashvili, 2020). Panel e shows Auroral Electrojet Upper (AU) and Lower (AL) indices in blue and red curve, respectively, provided by SuperMAG. Panel f shows the *Dst* index as black curve and K_p index as bar plots, provided by World Data Center for Geomagnetism, Kyoto, Japan and GFZ German Research Center for

10.1029/2024SW003938

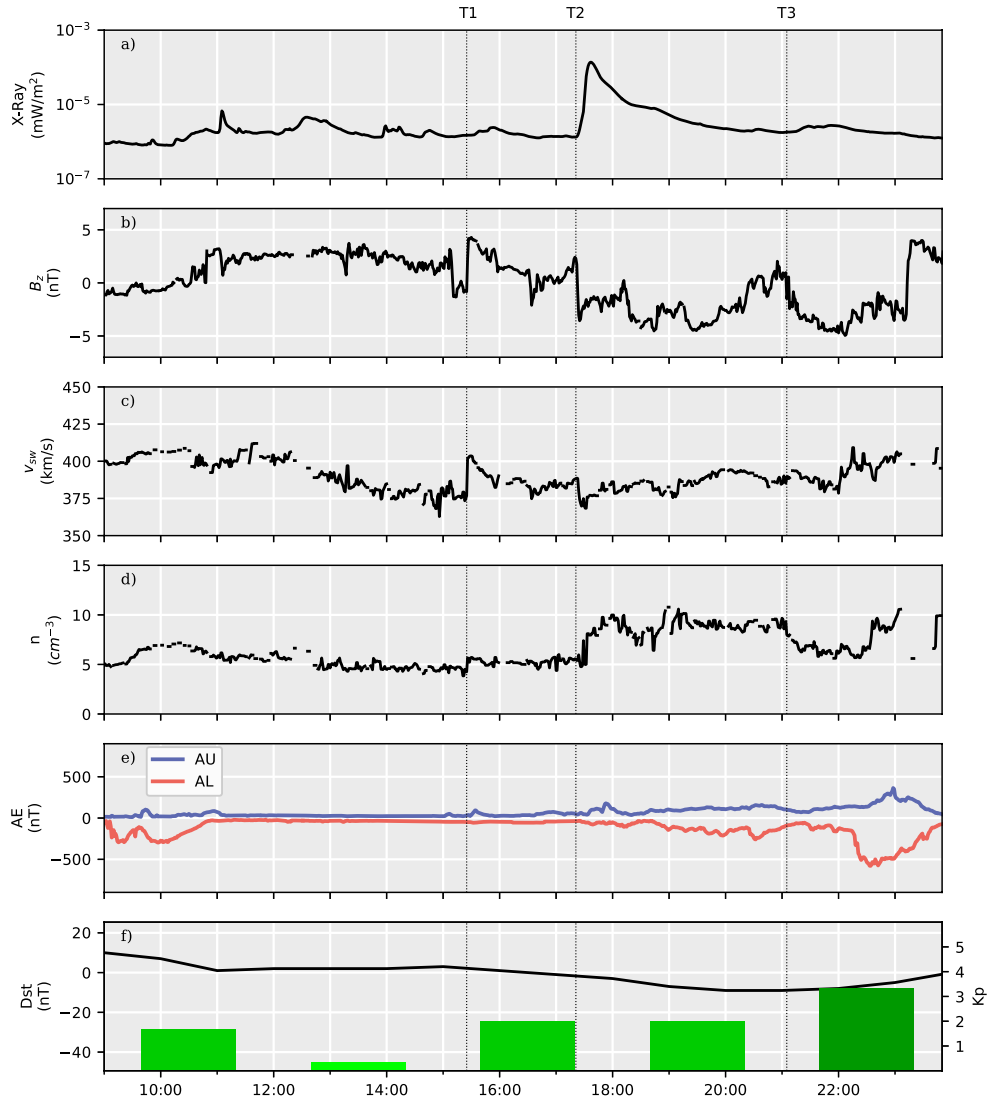

Figure 3. Solar geophysical parameters during 30 March 2022, (a) X-ray energy flux integrated between 0.1 and 0.8 nm wavelengths; (b) interplanetary magnetic field B_z component; (c) Solar wind speed; (d) Solar wind density; (e) Auroral Electrojet Indices, Upper (AU) and Lower (AL) indices are plotted by blue and red curves, respectively; (f) Disturbance Storm-time (Dst) index and Planetary-K (Kp) index plotted by black curve and green bars respectively. Vertical dotted lines labeled as $T1$, $T2$, and $T3$ marks a weak magnetic cloud passage, the solar flare and the termination of IMF B_z oscillations, respectively.

Geosciences, respectively. Vertical dashed lines T1 and T3 demonstrate two geoeffective events and T2 marks the onset of the solar flare.

The solar flare erupted from active region AR12975, located at N13W52, on 30 March 2022. According to GOES measurements, the flare onset is recorded at 17:21 UT, marked as T2 for future reference in Figure 3. The subsolar point is located around 78°W at the flare onset. The peak flux, observed at 17:37 UT, is 1.3×10^{-4} W/m^2, classifying the flare as an X1.3 event. Preceeding this event, 10 C-class solar flares erupted within the same day from the same active region with no observed M-class flare.

We selected a period spanning from 09:00 UT to 23:45 UT on the same day for detailed analysis. The geomagnetic field and the solar wind activity were overall quiet. T1 represents the termination of a 20-min period during which abrupt changes in B_z occurred. The solar wind speed surged and the solar wind density exhibited a weak increase after T1, indicative of the passage of a weak interplanetary magnetic cloud. This phenomenon can be associated with the arrival of the earth-directed component of the coronal mass ejections launched a day earlier.

The IMF B_z component was predominantly northward until the flare onset (T2) and turned southward afterward, fluctuating between ±5 nT. The solar wind speed fluctuated around 360–410 km/s. The solar wind number density was around 5 particles per cm^3 before T2 and 10 particles per cm^3 after the flare peak. T3 represents the time when IMF B_z oscillated significantly, and the solar wind density started recovering to preflare values. Notably, just before T3, multiple direction reversals of B_z took place. Both AU and AL indices remained at quiet levels until the flare, except for an elevation of AL index in the early hours. Subsequent to the flare event, both AU and AL indices were gradually elevated. After T3, both indices reached their maximum values; however, the AL index peaked nearly half an hour earlier than the AU index. The maximum K_p index of 3+ coincided with the maximum of auroral electrojet indices. The *Dst* index reached its minimum value ∼1 hr earlier.

2.4. Numerical Modeling Approach

The Global Ionosphere and Thermosphere Model (GITM) is a three-dimensional first-principle nonhydrostatic general circulation model simulating the T-I assuming a two-way coupling between the ions and neutrals. It explicitly solves the continuity, momentum, and energy equations in a spherical coordinate system to calculate the density, velocity, and temperature of neutrals, ions, and electrons (Ridley et al., 2006). GITM has a flexible grid size and can use a stretchable grid in latitude and altitude. The altitude range extends from ∼100 to ∼600 km. GITM relaxes the hydrostatic assumption in the vertical direction, which allows for the evaluation of non-hydrostatic impacts (e.g., propagation of acoustic-gravity waves) on the T-I system. GITM also includes a self-consistent electrodynamo solver for the mid- and low-latitudes (Vichare et al., 2012). The ionospheric convection in GITM is specified by the Weimer (2005) model. Auroral particle precipitation in GITM is specified by the empirical FTA model (Wu et al., 2021). GITM has been used to study various aspects of thermosphere-ionosphere coupling, for example, the effects of electric field variability, model resolution, and ion-neutral flow differences on the Joule heating (Deng & Ridley, 2007; Yiğit & Ridley, 2011a), thermospheric neutral vertical wind variability (Yiğit & Ridley, 2011b), and thermospheric dynamics during major magnetic storms (Yiğit, Frey, et al., 2016) and during solar flares (Pawlowski & Ridley, 2008).

Radiation with different wavelengths emanates from distinct depths in the solar atmosphere and is subsequently absorbed at varying altitudes within Earth's atmosphere. The FISM serves as an empirical model of the solar irradiance designed to address spectral and temporal gaps in satellite observations (Chamberlin et al., 2020). GITM utilizes FISM to better represent the solar radiation with different wavelengths entering the atmosphere. The original FISM data, characterized by a 1 Å spectral resolution across 0 to 1,900 Å spectral range, is binned into 59 wavelength intervals which are then used in combination with the ionization and heating cross sections specified by Torr et al. (1979) to calculate the ionization rates and thermospheric and ionospheric heating in GITM. These intervals cover solar fluxes and cross sections ranging from 1 to 1,750 Å and are distributed as follows: (a) 4 bins (1–16 Å) for X-rays, (b) 21 bins (16–950 Å) for UV, (c) 16 bin for (950–1,750 Å) Vacuum UV and (d) 18 bins for specific spectral lines corresponding to various transitions of Iron I, Magnesium II, Hydrogen I, Calcium II, Helium I and Oxygen I. Figure 4 shows the variation of these bins after the first 3 hr of the solar flare event, presented as the ratio of the flare-time flux (F_1) to the pre-flare fluxes (F_2). Pre-flare fluxes are computed as the median value of previous 2 hr before the flare onset. Following the flare onset, X-ray flux surged to 80 times the preflare flux, while the intensity of other wavelengths increased by a maximum of 2 times during this time.

In order to simulate a non-flare scenario with GITM, the FISM model was manipulated from flare onset to 3 hr afterward to suppress the irradiance enhancements caused by the solar flare. The manipulation was done by replacing the solar radiation of all wavelengths with their pre-flare values. GITM was run four times in this study under the conditions given in Table 1. The benchmark run (EXP0) used the actual FISM solar flux along with the realistic IMF inputs. In the no-flare run (EXP1), the solar flare effects were suppressed by using the manipulated FISM solar flux values. In the northward IMF run (EXP2), the real FISM values were used similarly to EXP0, but the southward turning of IMF B_z is suppressed by maintaining a value of +2 nT from the solar flare onset to the end of the day. Finally, an all-quiet run (EXP3) utilized both the modified solar spectra and modified IMF B_z. These experiments are summarized in Table 2. The difference between EXP1 and EXP3 reflects the isolated effects of the southward turning of the IMF B_z, while the difference between EXP2 and EXP3 reflects the isolated effects of the solar flare. On the other hand, the difference between EXP0 and EXP3 reflects the effects driven by the (linear) combination of the solar flare and the southward turning of the IMF B_z. Subtracting the sum of the isolated effects of the solar flare (EXP2 − EXP3) and the southward turning of the IMF B_z (EXP1 − EXP3) from

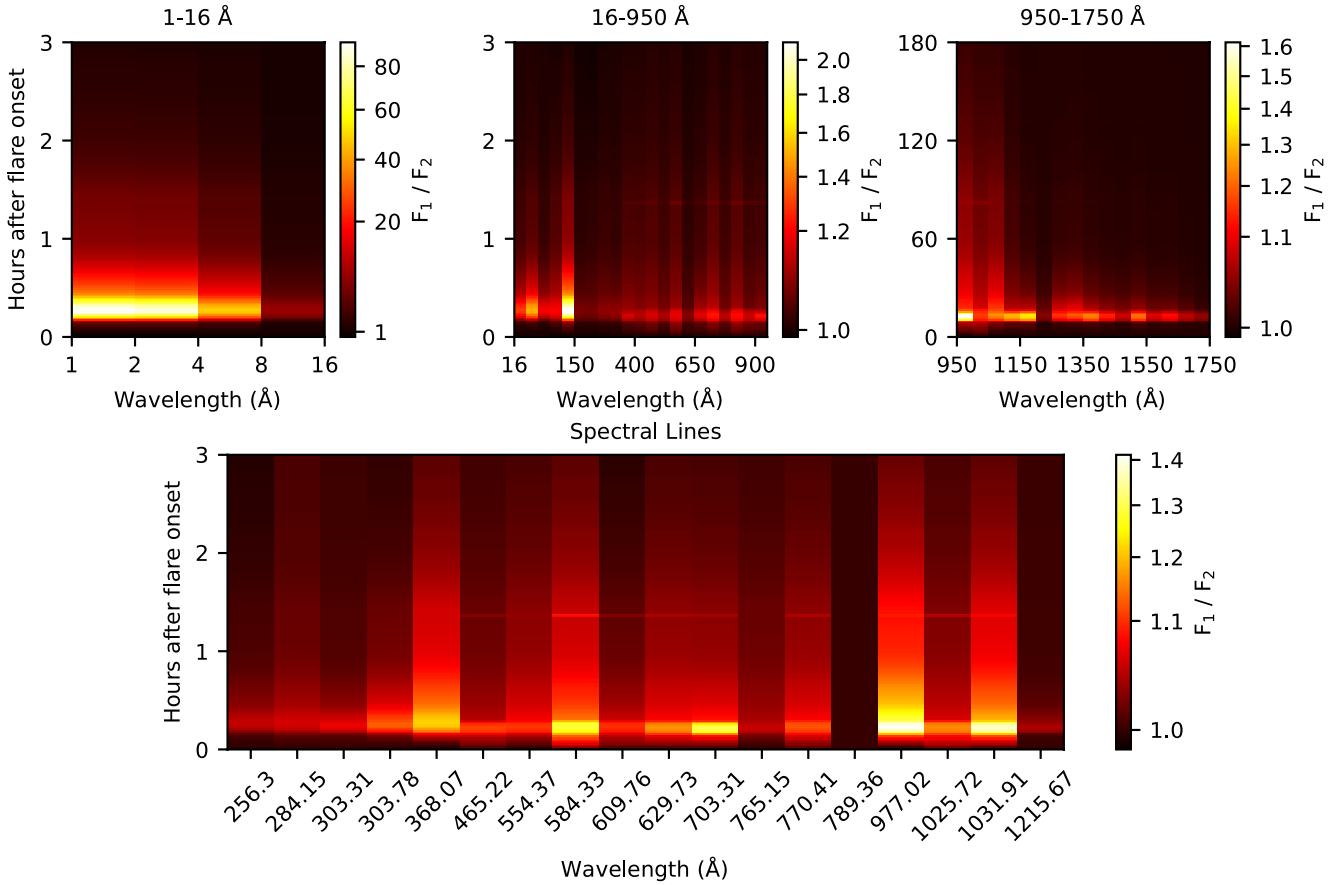

Figure 4. Flux enhancements according to the Flare Irradiance Spectral Model after the first 3 hr of the flare onset. Enhancements are presented as the ratio of the flare-time flux (F_1) to the pre-flare fluxes (F_2). Flux values are binned into 59 wavelength intervals according to utilization in Global Ionosphere Thermospere Model.

their combined effects (EXP0 − EXP3) will reflect the effects of their interaction (nonlinearity), calculated by (EXP0 − EXP3) − (EXP1 − EXP3) − (EXP2 − EXP3). These calculations are summarized in Table 3. The model starts on 28 March 2022 to allow stabilization, and outputs before 30 March 2022 are discarded. All simulations used realistic auroral electrojet inputs to drive the particle precipitation model (Wu et al., 2021), ensuring that all runs had identical precipitation effects of energetic particles.

Table 1
GITM Conditions Used in This Study

Condition	Value
Resolution (latitude × longitude)	2.5° × 5°
Resolution (altitude)	1/3 × scale height
Eddy diffusion coefficient	300
Eddy pressure levels (lower, upper)	0.0050, 0.0005
Heating efficiency (Photoelectron, neutral)	0.00, 0.05
Thermal conduction (molecular)	5.6×10^{-4}
Thermal conduction (atomic)	7.6×10^{-4}
Thermal conduction power	0.72
Dynamo high latitude boundary	65°

3. Results and Discussion

3.1. Total Electron Content Variations During the Solar Flare

Figure 5 presents the dTEC keogram for CONUS. From 10:00 UT to 14:00 UT, the passage of the ST is evident. The meridional speed of the ST is approximately 460 m s^{-1}, akin to Earth's rotation speed. The meridional width of ST is ∼1700 km. These ST characteristics align with previously published values (Afraimovich et al., 2010).

Following the ST passage, discernible quasi-periodic, eastward moving dTEC disturbances are observed across the CONUS. A phase reversal (from positive to negative dTEC) becomes apparent after 13:00 UT in the eastern part of the region. One hour later, the eastern region reverses again to positive dTEC values, while the western region predominantly displays negative dTEC until T1. Subsequent to T1, synchronized global oscillations persist prominently for approximately 1 hr. Although the periodicity is evident,

Table 2
Nomenclature for GITM Simulations

Label	Name	Description
EXP0	Benchmark Run	Realistic solar spectra and realistic IMF B_z
EXP1	No-Flare Run	Modified (quiet) solar spectra and realistic IMF B_z
EXP2	Northward IMF Run	Realistic solar spectra and modified (quiet) IMF B_z
EXP3	All-Quiet Run	Modified (quiet) solar spectra and modified (quiet) IMF B_z

phase progression in longitude is absent for these oscillations. Similar phenomena observed under minor solar-geomagnetic disturbances are reported by S.-R. Zhang et al. (2023). These authors concluded that the possible causative factor behind simultaneous global ionospheric disturbances is penetration electric fields of solar-geomagnetic origin.

The solar flare response becomes pronounced after T2, characterized by an initial drop followed by an enhancement of dTEC. The initial drop, spanning half the length of the filter window is an artifact of the Savitzky-Golay filter as described in Section 2. After the flare, dTEC exhibits synchronized variations across the CONUS, gradually dampening until 19:00 UT. Shortly after 19:00 UT, disturbances in the eastern region diminish, while positive dTEC disturbances emerge in the western region. The propagation direction of the post-flare disturbances are predominantly eastward until T3 (Figure 5, black arrows). Nevertheless, westward propagation is recognized between 115° and 130°W.

At T3, another phase reversal (positive to negative dTEC) is introduced, lasting until 22:00 UT across the CONUS. After 22:00 UT, the magnitudes of the disturbances in the eastern region are elevated, revealing westward propagation between 80° and 100°W. This period after 22:00 UT coincides with the maximum of auroral electrojet activity (see Figure 3e).

Overall, Figure 5 reveals a longitudinal response beginning approximately 1 hr after the solar flare onset, with enhanced disturbances in the western region. This asymmetry continues until 22:00 UT and reverses afterward, with disturbances in the eastern region enhanced. On the other hand, dTEC magnitudes around 105°W are consistently weaker compared to the eastern and western sides of this longitude.

The longitudinal solar flare response is further analyzed by locally comparing the results. The region between 30° and 50°N latitudes and 90° ± 0.45°W longitudes is designated as the East CONUS and the region between 30° and 50°N latitudes and 120° ± 0.45°W longitudes is designated as the West CONUS. There is a disparity in GNSS receiver coverage across the CONUS. Our data set includes measurements by 1,127 unique receivers in the West CONUS and 514 in the East CONUS, whereas there are 253 at 105° ± 0.45°W longitudes. However, this difference is partly mitigated by the interpolation scheme explained in Section 2.1; in the 3D spatiotemporal domain of the dTEC data set, at least one measurement is captured by 81% of the pixels in the East CONUS and 99% in the West CONUS. This ratio is 87% at 105° ± 0.45°W longitudes. Note that the pixel coverage is higher, the receiver count is lower at 105° ± 0.45°W longitudes compared to the East CONUS. This relationship between pixel coverage and GNSS receiver count arises from the box filter kernel, which is influenced by the irregular distribution of receiver locations.

Table 3
Calculations Performed on GITM Simulations

Calculation	Description
EXP0–EXP3	Combined effects of IMF B_z and solar flare
EXP1–EXP3	Isolated IMF B_z effects
EXP2–EXP3	Isolated solar flare effects
(EXP0–EXP3)–(EXP1–EXP3)–(EXP2–EXP3)	Interaction of IMF B_z and solar flare

10.1029/2024SW003938

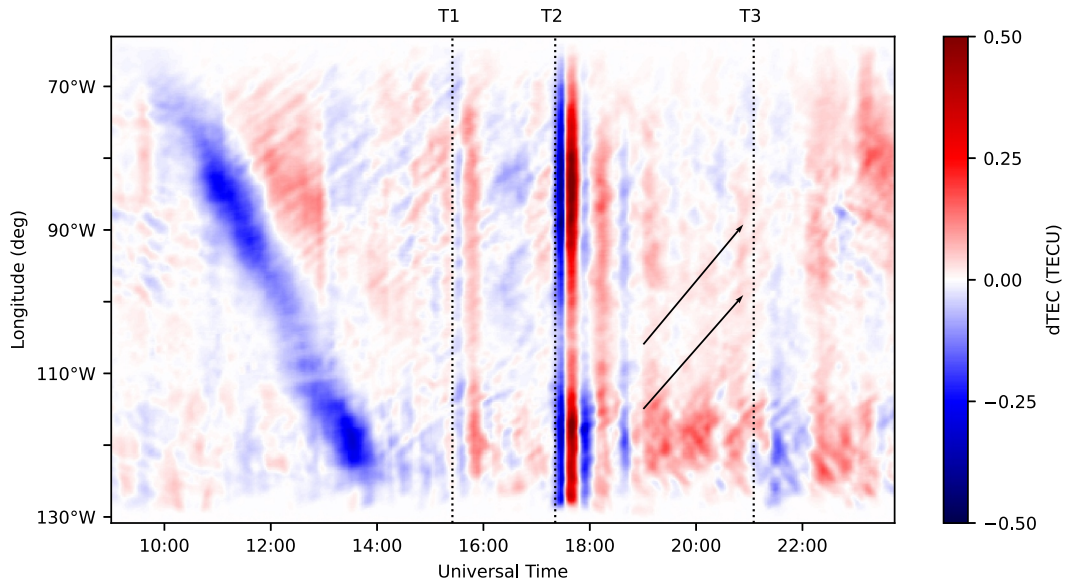

Figure 5. Overview of the latitude-averaged detrended total electron content (dTEC) as a function of time and longitude from 09:00 UT to 23:45 UT. The keogram combines the dTEC variations within 63–131°W and 23–55°N. The passage of the solar terminator is evident as the westward propagation of the negative dTEC values until 14:00 UT. Vertical dotted lines labeled as *T*1, *T*2, and *T*3 mark space weather events (See Figure 3) effective on dTEC. Black arrows are drawn parallel to the propagation direction of post-flare disturbances.

Figure 5 reveals that the magnitudes in the East CONUS are higher following the solar terminator, but lower following the solar flare compared to the West CONUS. Furthermore, the dTEC magnitudes are consistently weaker across the 105° ± 0.45°W longitudes, despite this region having a higher pixel coverage ratio than the East CONUS. These findings suggest that the effects of the differences in pixel coverage of the East and West CONUS on the temporal variation of dTEC are negligible.

The East–West asymmetry is quantified using the method described in Section 2.2. Local frequency contents along with the temporal variation of the keograms for the East and West CONUS are shown in Figures 6 and 7, respectively.

The ST-passage in the East CONUS, observed between 11:00 and 12:00 UT, causes slight enhancement of the spectral powers for all periods (Figure 6a). Two hours after the ST-passage, around 14:00 UT, equatorward-moving ST-induced wavefronts are observed (Figure 6b). The dominant oscillation periods of ST-induced waves reported as 90–120 min by Galushko et al. (1998) exceeds the analyzed periodicity range of our study. The time shift of the wavefront occurrences reported as 1.5–2.5 hr after the ST appearance by Afraimovich (2008) aligns with our findings.

The ST passage is observed in the West CONUS between 13:00 and 14:00 UT (Figure 7). A comparison of the mean spectral power during the ST passage between the East and West CONUS, reveals that the response is 40% stronger in the West CONUS. Following the ST passage, quasi-periodic pulsations of the spectral power continue until T1 in the West CONUS for all periods, although in different phases. In contrast, spectral power in East CONUS returns back to the background values following the ST passage, except a weak enhancement in all periods around 13:00 UT. ST-induced TIDs in the West CONUS appear after 16:00 UT (Figure 7b, black arrows) due to the 1.5–2.5-hr time delay required for their formation. Between T1 and 16:00 UT, mean spectral power is 29% higher in the West compared to the East CONUS. In other words, the East–West asymmetry decreases after T1 compared to the ST passage, suggesting that the spectral power in the East CONUS is positively contributed by the ST-induced TIDs, while the ST-induced TIDs in the West CONUS have yet to form.

The time localization of periodic content in a wavelet transform becomes increasingly imprecise with longer periods due to the windowing effects (Appendix A). In other words, there is an intrinsic uncertainty between the horizontal and vertical axis. Specifically, a wavelet window at higher periods covers a longer width on the time

10.1029/2024SW003938

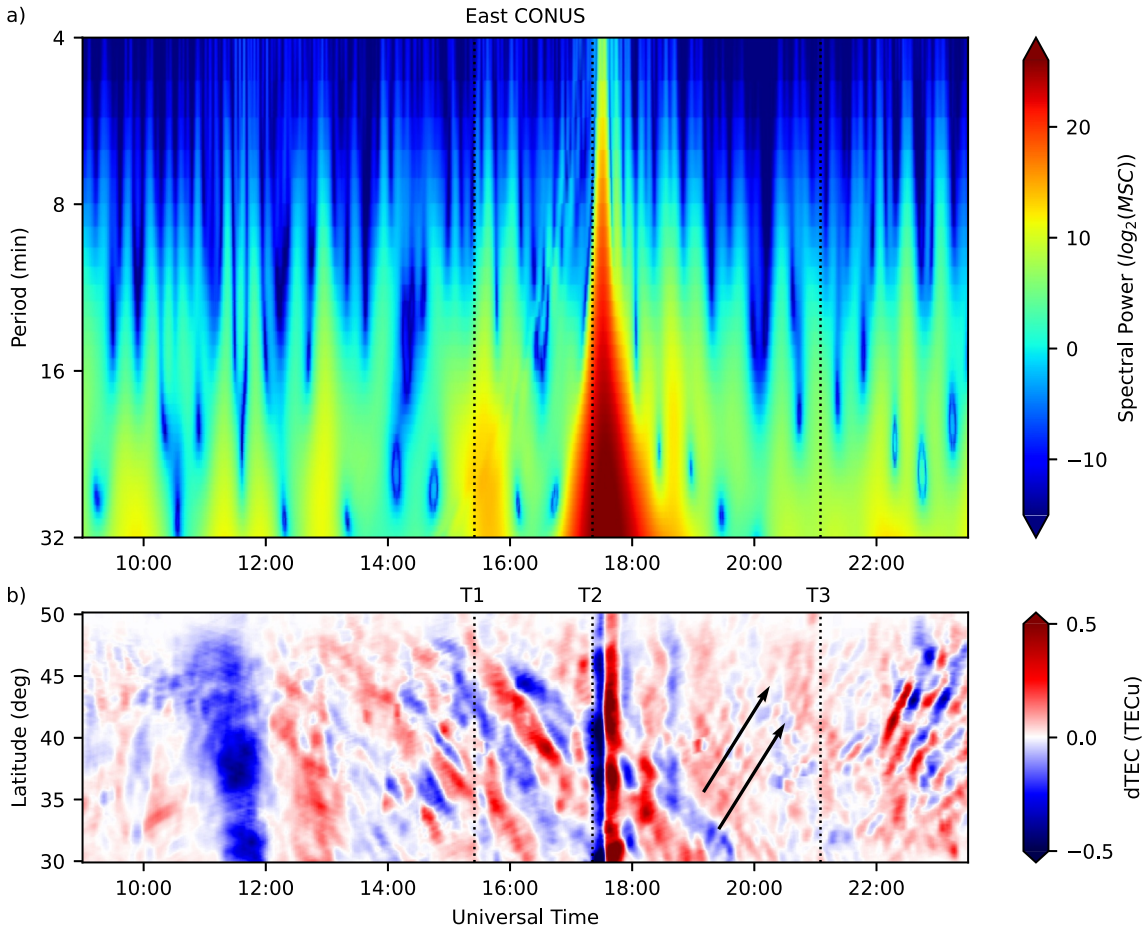

Figure 6. Wavelet Coherence results for the East Conus which spans the longitude −90.5° W ± 0.45 between 30°N and 50°N latitudes (a). Periodicity variations are given as spectral power in terms of the magnitude-squared coherence (MSC). Vertical dotted lines labeled as T_1, T_2, and T_3 mark space weather events (See Figure 3) effective on dTEC. The precision of the temporal localization for coherent oscillation enhancements get weaker with increasing periods due to the trade-off between time localization and period localization (see text). Panel (b) shows the longitude-averaged dTEC variations for the same region. Black arrows are drawn parallel to the propagation direction of post-flare disturbances.

axis but a smaller width on the period axis compared to a wavelet window at smaller periods. This uncertainty causes the spectral power variations in longer periods related to the T1, T2 or T3 to appear earlier then the corresponding event in Figures 6 and 7.

After the solar flare (T2), Figures 6a and 7a reveal enhancements of spectral power across all periods, lasted until 19:00 UT. Between T2 and 19:00 UT, mean spectral power across all periods is only 1% stronger in the West compared to the East CONUS. Hence the East–West asymmetry vanishes, as the East CONUS is closer to the subsolar longitude during the flare onset (78°W). The asymmetry is even reversed for 4–8 min periods; the mean spectral power in the East CONUS between T2 and 19:00 UT is 24% higher compared to the West CONUS, suggesting a stronger solar zenith angle dependence for the ionospheric disturbances with lower periods.

Solar flare-triggered global dTEC oscillations last until 19:00 UT (Figures 6b and 7b). After 19:00 UT, solar terminator-triggered, equatorward-moving TIDs in the East CONUS leave the analyzed region, while those in the West CONUS are enhanced in terms of wavelength and magnitude (Figure 7b, black arrows). Notably, northward moving waveforms begin forming in the East CONUS after 19:00 UT (Figure 6b, black arrows). The mean spectral power in the West CONUS is about 2.2 times higher during 19:00–22:00 UT, indicating that the solar flare's contribution to the East–West asymmetry is strongest compared to the other events (ST or T1).

The sequential 2D dTEC maps in Figure 8 illustrate TID emergence and propagation between 22:00 UT and 23:00 UT around the East CONUS. Weak wavefronts initially appeared around 42°N 85°W at 22:00 UT. Thirty minutes later, multiple wavefronts of the TID, elongated NE–SW and separated ∼1° longitude, became discernible. By

10.1029/2024SW003938

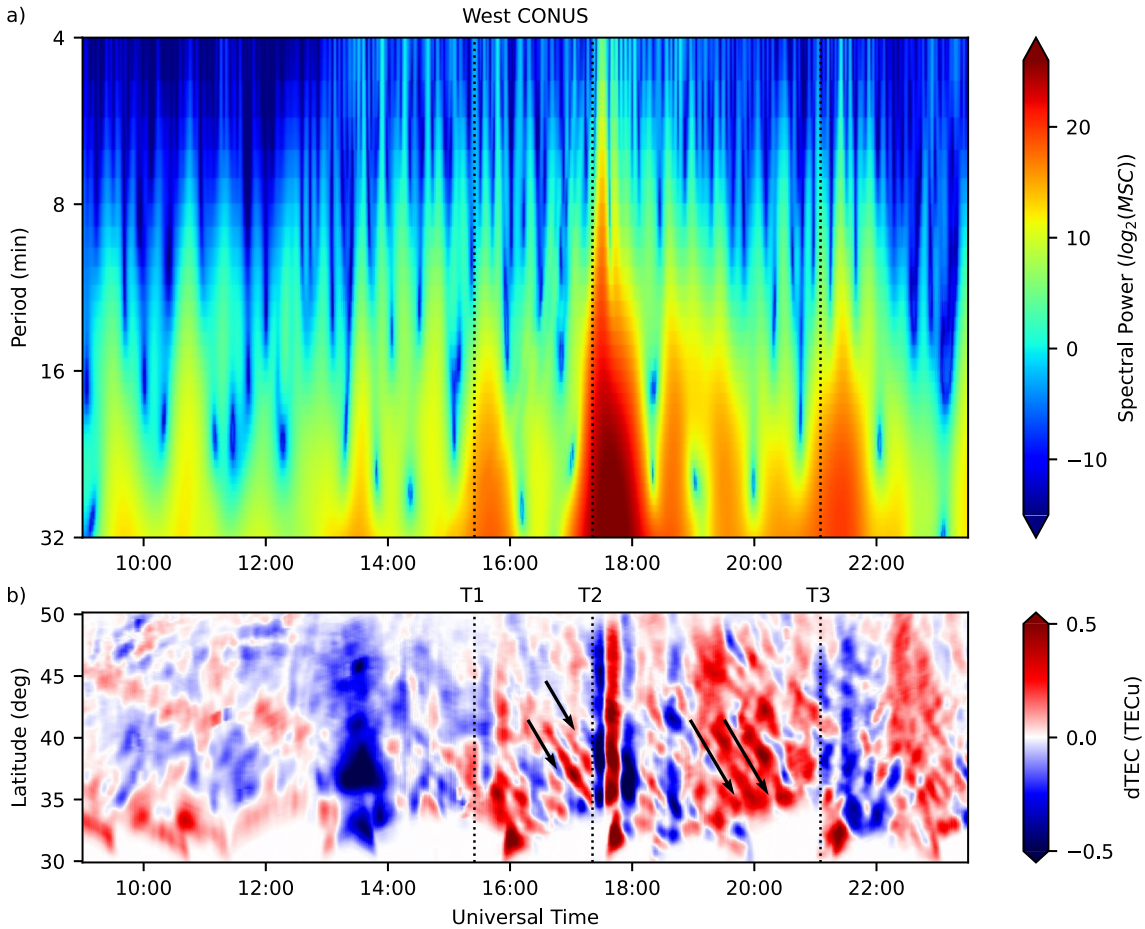

Figure 7. Same as Figure 6 but for the longitude −120.5°W ± 0.45 (West CONUS). Black arrows are drawn parallel to the propagation direction of post-sunrise and post-flare disturbances.

23:00 UT, the horizontal extend of the TID wavefronts expanded significantly. The TID, which is also apparent in Figure 7 after 22:00 UT, introduced an increase to the spectral power in the East CONUS. The East–West asymmetry vanished following the TID emergence; the mean spectral power in the West CONUS is only 16% stronger after the TID emergence compared to 220% before.

TID propagation is further analyzed using cross correlation. A 2-hr period centered at 22:30 UT is selected to study the zonal and meridional propagation of TIDs. Figure 9 shows westward propagation with a horizontal phase speed of 250 m s^{-1} and bimodal northward propagation with phase speeds of 150 and 260 m s^{-1}. Horizontal wavelengths are approximately 230 km and the period is 67 min. These measured characteristics are indicative of Medium Scale TIDs (MSTIDs).

The ability of solar flares to trigger TIDs is a topic of ongoing debate. Qian et al. (2019) conducted model simulations and data analysis to investigate T-I responses to two solar flares, both larger than X8, during a major geomagnetic storm in September 2017. They concluded that solar flares alone were not sufficient to excite TIDs, although they did alter the amplitudes and propagation speeds of existing disturbances. This aligns with our findings in the West CONUS (Figure 7), where solar terminator-triggered TIDs are modulated in wavelength and magnitude following the solar flare. Conversely, S.-R. Zhang et al. (2019) examined TEC perturbations associated with an X9.3 solar flare, also occurring during the September 2017 geomagnetic storm. They reported post-flare TIDs coexisting with solar terminator-triggered TIDs. These post-flare TIDs persisted for over 5 hr and predominantly propagated eastward, though their distinction from solar terminator-triggered TIDs was not clear. Our findings support the eastward propagation of TIDs during the 5 hr following the solar flare, particularly between 90° and 120°W (Figure 5, black arrows). On the contrary, the observed westward propagation in the

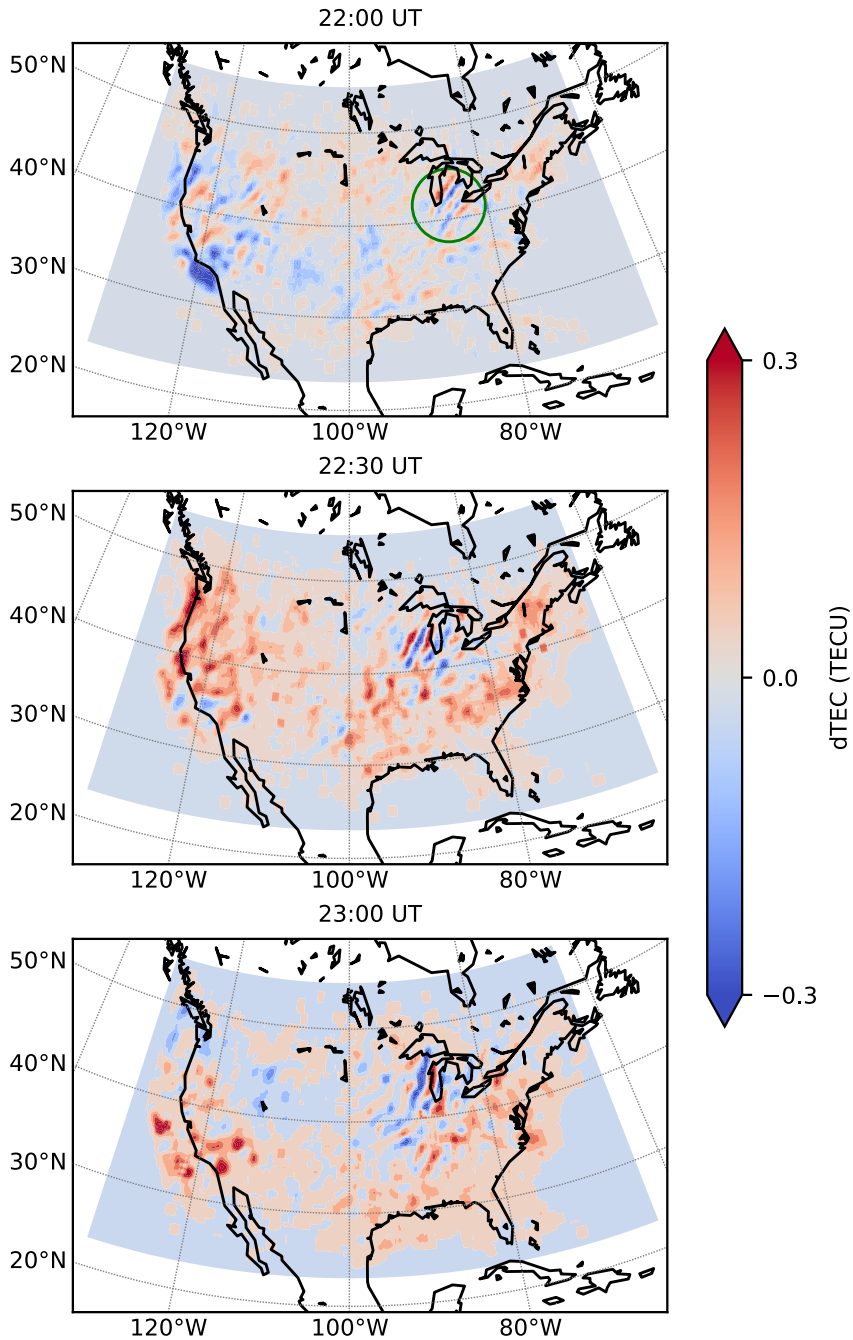

Figure 8. Two-dimensional dTEC maps indicating the occurrence and propagation of traveling ionospheric disturbances from 2200 UT to 2300 UT. The maximum amplitude of the absolute dTEC is saturated at 0.3 for better visualization. First appearance of wavefronts at 22:00 UT are indicated by the green circle.

West CONUS particularly between 120° and 130°W can be linked to the variations in global electric fields during the solar flare (Chen et al., 2021), considering the polarization electric fields embedded in solar terminator-triggered TIDs (S.-R. Zhang et al., 2021). Longitudinal variation of the electrodynamics response triggered by solar flares (Manju et al., 2009; Sripathi et al., 2013) may be a possible factor responsible for the preference of West CONUS for westward propagation.

We explicitly observe poleward propagation in the East CONUS (Figure 6b, black arrows) after 19:00 UT. Habarulema et al. (2018) reported poleward TIDs launched from the geomagnetic equatorial region as a result of

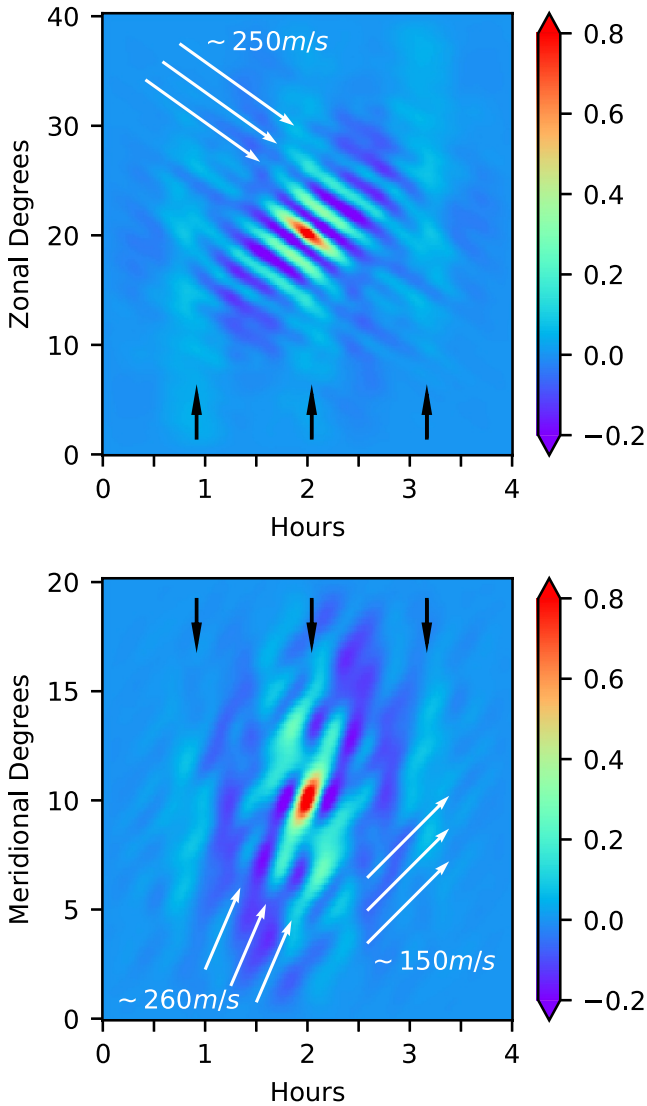

Figure 9. Cross-correlation analysis results used to estimate disturbance traveling velocities and periods. The upper panel shows the results for zonal propagation at 42.5°N ± 0.6° within the longitude range of −100 to −80°W between 21:30 and 23:30 UT. Zonal degrees increase toward east. White arrowhead lines, parallel to the bright bands of high cross-correlation, indicate synchronized westward propagation with a phase speed of 250 m/s. Black arrowhead lines mark the oscillation period, centered at 67 min. The lower panel shows a similar analysis at −90°E ± 0.6° within the latitude range of 37.5° to 47.5°N between 21:30 and 23:30 UT, indicating bimodal northward propagation.

increased Lorentz coupling due to the penetrating electric field during the southward turning of the IMF. J. Liu et al. (2021) reported solar flare-induced penetration electric fields, triggered by the instantaneous conductance enhancements during the solar flare. Thus, the poleward propagating wave forms in our results in the East CONUS can be linked to the penetration electric fields. Additionally, enhanced penetration electric fields associated with rapid changes in IMF B_z (K. Zhang et al., 2019) at T3 may contribute to the TID emergence afterward at the East CONUS.

On the other hand, Jonah et al. (2018) associated the poleward propagating TIDs observed during geomagnetically quiet days to lower atmosphere-ionosphere coupling via convectively generated gravity waves (GWs). Recent general circulation modeling efforts showed that internal GWs with large intrinsic phase speeds can propagate from the lower atmosphere to F-region altitudes and produce a significant amount of body force there (Yiğit et al., 2021). Thus, the direct effects of the forcing from below on the dTEC results cannot be ruled out.

3.2. General Circulation Modeling and Density Variations

We now turn our focus to theoretically explore the factors contributing to the asymmetric response of the CONUS during and after T2 (solar flare onset, 17:21 UT). For this purpose, we utilized four simulations (as detailed in Tables 1–3), designed to investigate the large-scale longitudinal response of the T-I system. The comparison of simulated and observed TEC results (Figure 10) suggests that GITM qualitatively reproduced the East–West TEC asymmetry over the CONUS (S.-R. Zhang et al., 2011), specifically showing a higher TEC magnitude in the West CONUS compared to the East.

We begin our analysis by calculating the asymmetry index of the key scalar T-I parameters (neutral density, O/N2 ratio, and electron density) between the West CONUS (120°W, 40°N) and East CONUS (90°W, 40°N) following the procedure outlined in S.-R. Zhang et al. (2011) and Zhao et al. (2013). The asymmetry index, R_{WE}, representing the west-to-east percentage difference, is calculated as $R_{WE} = (S_{West} - S_{East})/(0.5 \times (S_{West} + S_{East}))$, where S is any field variable in a specific simulation run. The results for EXP3 (all-quiet run) are presented in Figures 11a–11c. Positive values indicate higher values at the West CONUS, while negative values indicate higher values at the East CONUS. The R_{WE} for neutral density (Figure 11a) and O/N2 ratio (Figure 11b) reach their maximum before T2 (flare onset, 17:21 UT), favoring the East and West CONUS, respectively, and then almost stabilize throughout the day at higher altitudes. The R_{WE} for neutral density at lower altitudes enhances in favor of the West CONUS, especially after T2. The variations through the end of day reflect the upcoming sunset effect. Figure 11c reveals that R_{WE} for electron density at higher altitudes reverses from favoring the East CONUS to favoring the West CONUS after 16:00 UT, while this reversal takes place around 21:00 UT at lower altitudes.

The effects of the southward IMF Bz, the solar flare, and their nonlinear interaction are determined according to the calculations given in Table 3. The main effect of the IMF Bz forcing on the R_{WE} for the neutral density and the O/N_2 ratio is resiprocal, favoring the West CONUS and East CONUS respectively. This pattern is briefly reversed at altitudes above 200 km between 19:30 and 20:00 UT and around 200 km afterward (Figures 11a′ and 11b′). For the electron density, the influence of IMF Bz favors East CONUS between 200 and 300 km and West CONUS above it (Figure 11c′). The solar flare forcing (Figures 11a″–11c″) is less pronounced compared to the southward IMF B_z forcing. However, their nonlinear interaction (Figures 11a‴–11c‴) introduces effects that are absent under isolated forcings before 19:00 UT and gradually increase afterward.

10.1029/2024SW003938

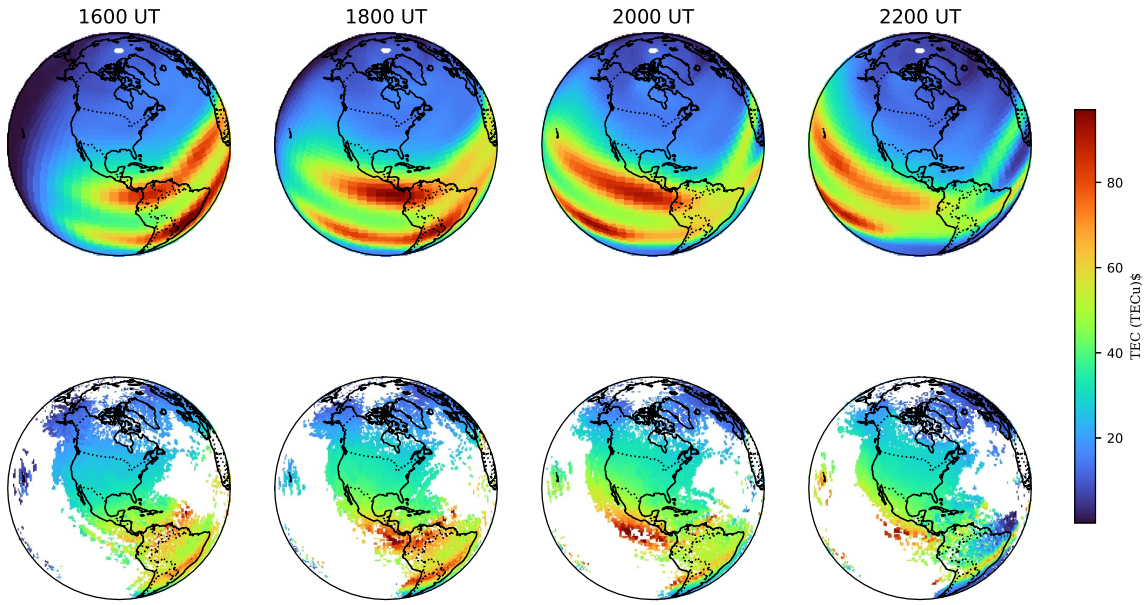

Figure 10. Comparison of simulated total electron content (TEC) (upper row) and observed TEC (lower row) at 2-hr intervals after 16:00 UT. TEC results are plotted on an orthographic projection centered at 90°W and 33°N.

A comparison of the vertical and meridional wind, as well as vertical ion drift, above the West and East CONUS as simulated in EXP3 (all-quiet run) is presented in Figure 12, given that the asymmetry index is not suitable for analyzing directional parameters. The effects of the southward IMF B_z, the solar flare, and their nonlinear interaction on these parameters are also illustrated in Figures 13 and 14 for the West and East CONUS, respectively.

The vertical wind above ~250 km is stronger in the West CONUS around and after T2 (Figure 12a′). IMF B_z forcing on the vertical wind is more pronounced in the East CONUS around 20:00 UT and after 22:00 UT (Figures 13a and 14a). The solar flare induces an enhancement in upward wind, which gradually diminishes over

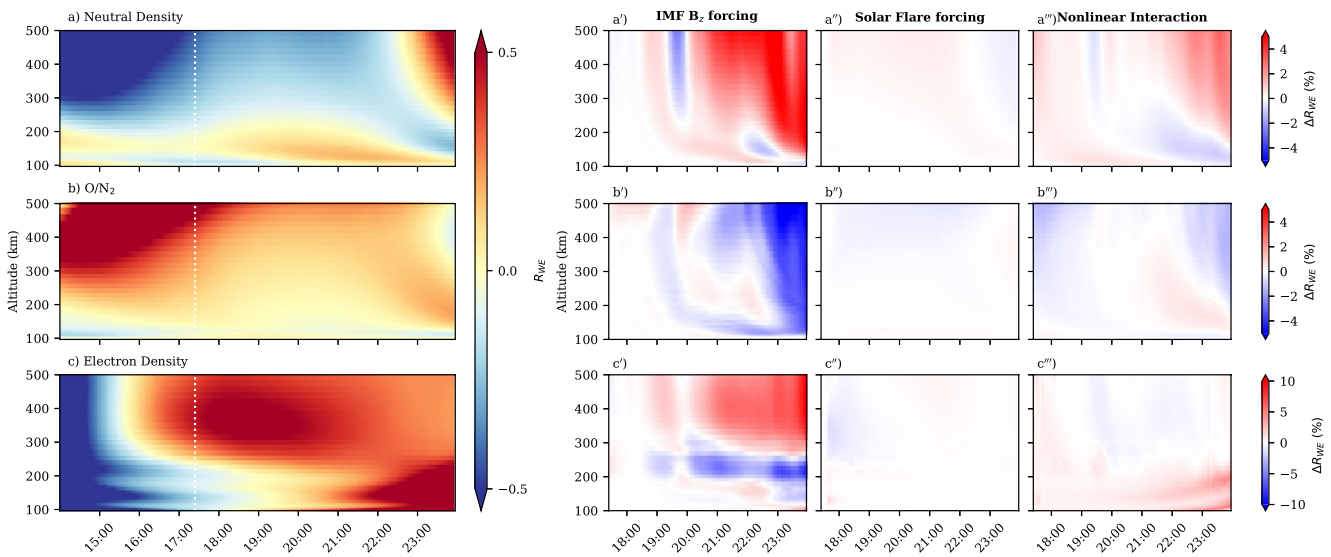

Figure 11. East–West asymmetry (R_{WE}) for the simulated neutral density (a), O/N_2 ratio (b) and electron density (c). Positive values indicate a higher value at the West CONUS (120°W, 40°N) and negative values indicate a higher value at the East CONUS (90°W, 40°N). The vertical dashed white line marks the solar flare onset (T2, 17:21 UT). Southward IMF B_z forcing, solar flare forcing and effects of their nonlinear interaction on the R_{WE} are presented in the second, third and fourth columns, respectively.

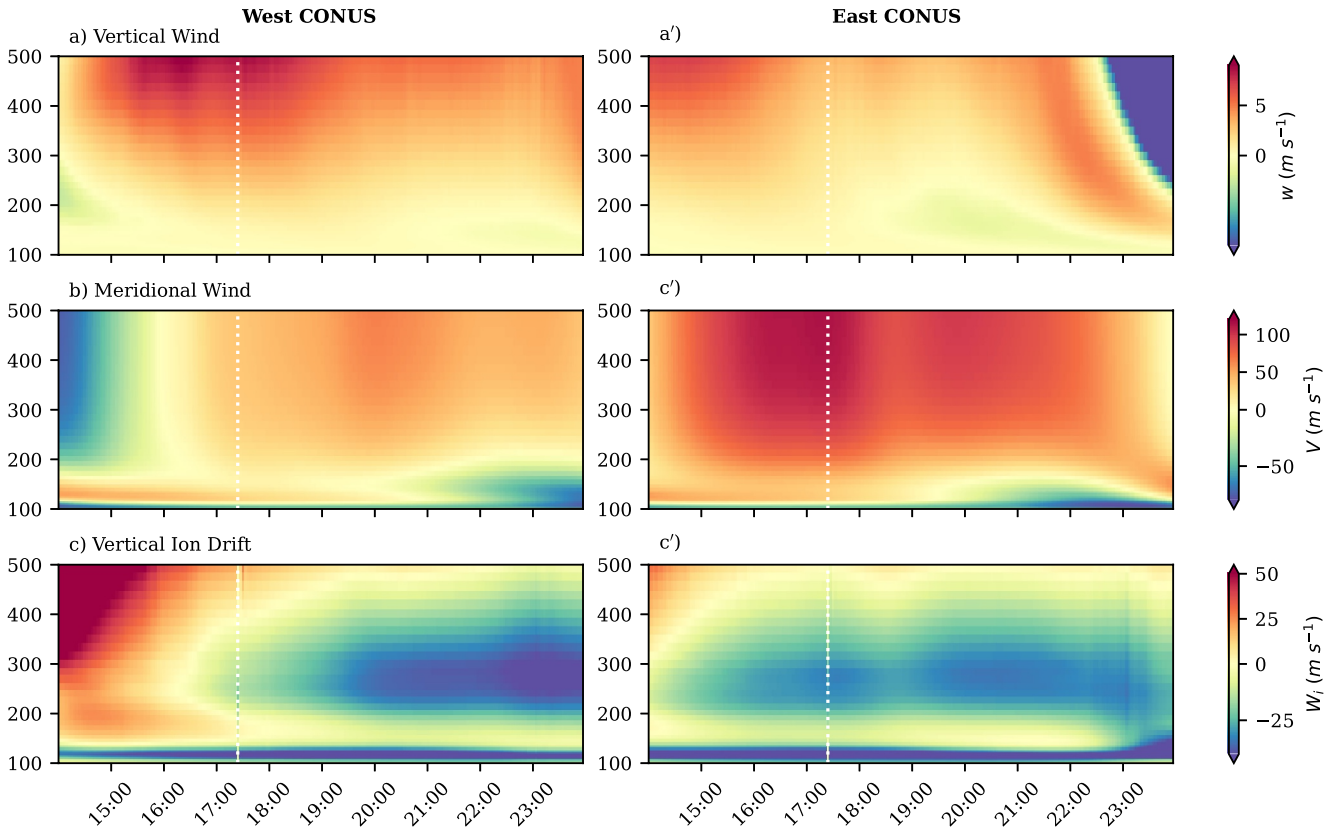

Figure 12. Comparison of the simulated vertical winds (a, a′), meridional winds (b, b′), and vertical ion drifts (c, c′) above the West CONUS (120°W, 40°N) and East CONUS (90°W, 40°N). Positive values indicate upward movement in the vertical direction and northward movement in the meridional direction. The vertical dashed white line marks the solar flare onset (T2, 17:21 UT).

approximately 2 hr after T2 for both regions. A weak upwelling enhancement can be observed in the East CONUS after 22:00 UT (Figures 13a′ and 14a′). The meridional (poleward) winds above 200 km are stronger in the East CONUS around and after T2 (Figure 12b′). The southward IMF B_z introduces equatorward forcing to the meridional winds after 19:00 UT, which is stronger above the West CONUS between 20:00 and 22:00 UT, and reverses after 22:00 UT above the East CONUS. The solar flare drives equatorward forcing to the meridional winds, though this effect is negligible in magnitude (Figures 13b′ and 14b′). The vertical (downward) ion drifts between 200 and 400 km are stronger in the East CONUS until 19:00 UT (Figure 12c′). IMF B_z forcing on the vertical ion drift is stronger in the East CONUS around 20:00 UT and after 22:00 UT (Figures 13c and 14c), similar to the vertical wind. However, both the vertical wind and ion drift show simultaneous upward enhancement above 200 km around 21:00 UT, suggesting ion-neutral coupling effects. The solar flare-driven upward ion drifts, pronounced at higher altitudes during the first hour after T2, are stronger in the West CONUS (Figures 13a′ and 14a′).

The nonlinear interaction between the southward IMF B_z and the solar flare introduces complex patterns in vertical wind and vertical ion drift, with similar pronounced rapid fluctuations continuing until the end of the event day (Figures 13a″, 13c″, 14a″, and 14c″). The nonlinear interaction in the meridional wind results in smooth, alternating poleward and equatorward deviations (Figures 13b″ and 14a″). The variations introduced by the nonlinearity are sporadically in opposite directions for all aforementioned variables above the West and East CONUS, suggesting a contribution to the asymmetric response.

The findings presented in Section 3.1 are supported by the GITM simulation results. Specifically, the maximum E–W asymmetry in dTEC variability occurs between 19:00 and 22:00 UT, favoring the West CONUS. The R_{WE} patterns for the O/N_2 ratio and electron density mirror this asymmetry, particularly at higher altitudes, underscoring the significance of background conditions in dTEC variability. Conversely, neutral density favors the West CONUS at lower latitudes, suggesting a potential contribution of vertical coupling to the East–West

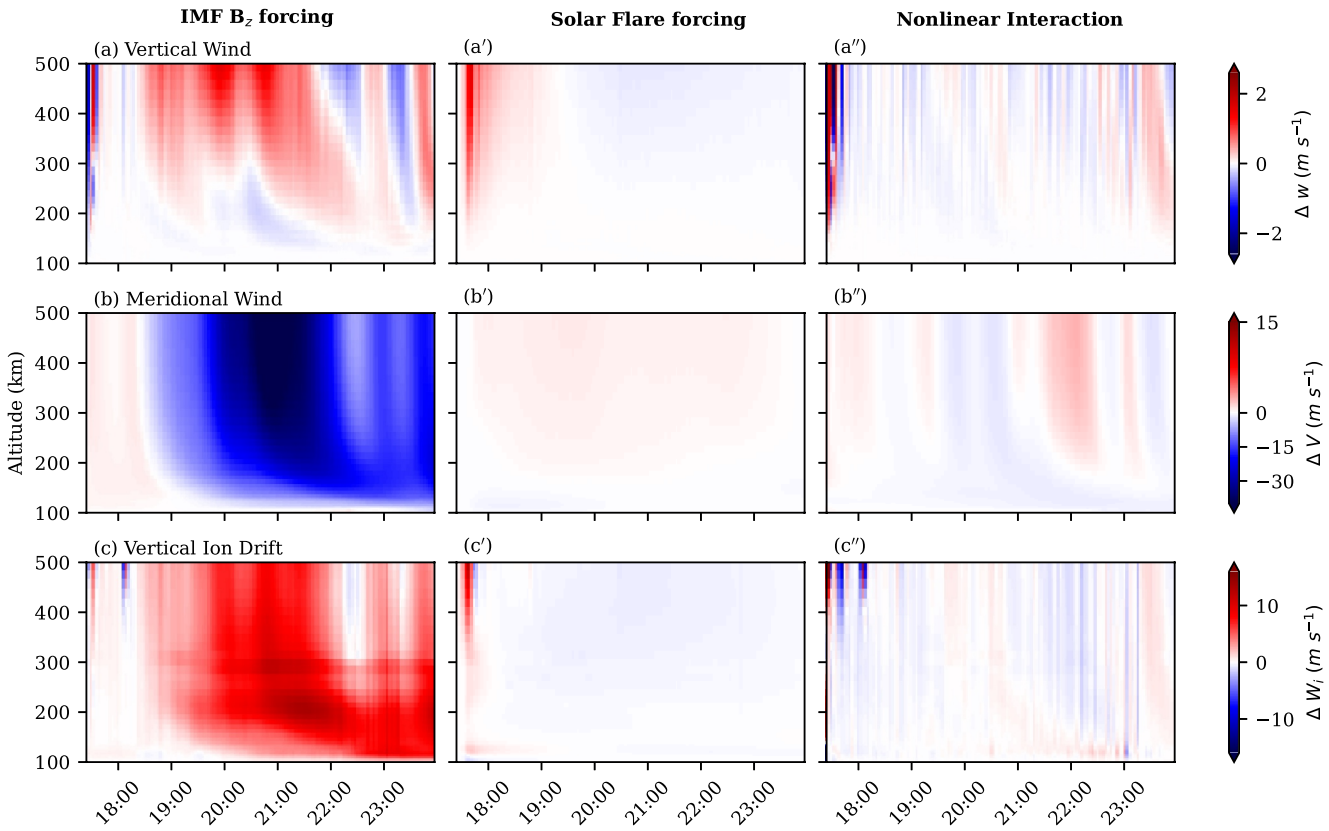

Figure 13. Influence of the southward IMF B_z (left column), solar flare (middle column) and their nonlinear interaction (right column) on the simulated vertical winds (a, a′, a″), meridional winds (b, b′, b″), vertical ion drifts (c, c′, c″) above the West CONUS (120°W, 40°N).

asymmetry, as further discussed in Section 3.3. Additionally, the stronger upwelling and downward ion drift in the West CONUS during the peak of the dTEC asymmetry highlight the importance of vertical dynamics. The GITM results indicate that the East–West asymmetry of the electron density is enhanced while the East–West asymmetries of the neutral density and the O/N_2 ratio are decreased after T2 due to the effects of the solar flare and the southward turning of the IMF B_z.

After T2, the East CONUS is in the afternoon-dusk sector, while the West CONUS is in the noon-afternoon sector. This local time difference lead to variations in solar heating patterns and temperature gradients, causing the West CONUS to experience greater barometric expansion compared to the East CONUS. Altitude differences in constant pressure levels between the East and West CONUS, driven by these variations in barometric expansion, may be responsible for the persistent R_{WE} of the neutral density at lower altitudes favoring the West CONUS (Figure 11a).

In an idealized case, Goldberg (1966) describe that, considering two stations with the same local time, the one with east (positive) declination will experience Lorentz force opposing gravity, while the one with west (negative) declination will experience a Lorentz force adding to gravity during the morning hours, and vice verse in the evening hours. The morning-to-evening variability is linked to the direction of global current system which is equatorward during the morning and poleward during the evening at Northern hemisphere midlatitudes. Considering their local times are already passed the noon time, the poleward component of the global current system at the East CONUS will be stronger, indicating a stronger Lorentz force compared to the West CONUS. Furthermore the East and West CONUS have negative and positive magnetic declinations, respectively (Alken et al., 2021). Thus, the Lorentz force is downward at the West CONUS but upward and stronger at the East CONUS during the studied time range. This pattern may explain the asymmetry in the directional T-I quantities (Figure 12) and their asymmetric response after T2 (Figures 13 and 14). Similar diurnal patterns are observed across the midlatitude zones in the CONUS (S.-R. Zhang et al., 2011). More on

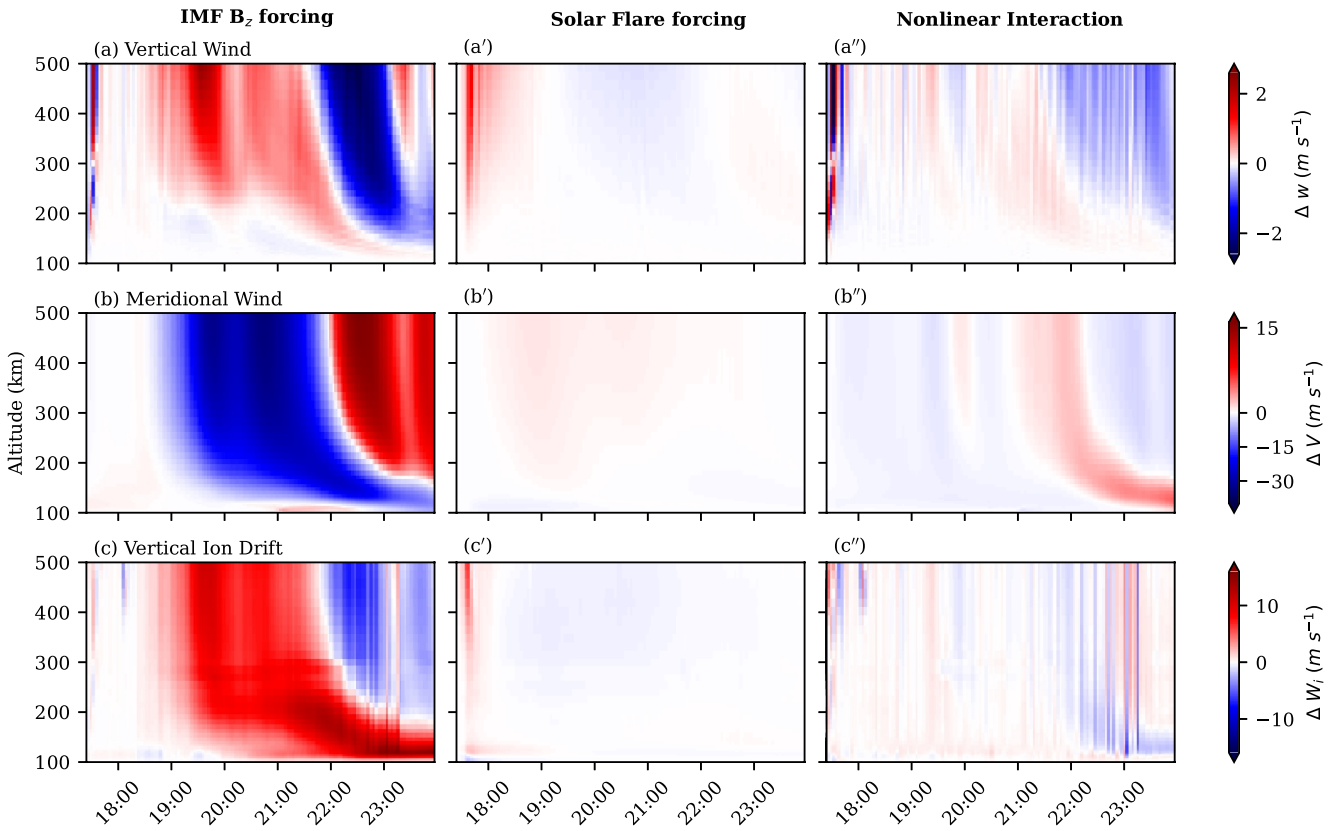

Figure 14. Same as Figure 13 but for the East CONUS (90°W, 40°N).

the magnetic declination effect in shaping longitudinal ionospheric variations at midlatitudes can be found in S.-R. Zhang (2021).

3.3. Analysis of Gravity Wave Influence on Longitudinal Asymmetry

We next analyze possible contribution of GWs to the longitudinal asymmetry. Vertical propagation of GWs within the dissipative T-I can be conceptualized as a dynamic interplay between dissipation and upward motion (Yiğit & Medvedev, 2010). The dissipation of GWs in this context is predominantly influenced by molecular viscosity and heat conduction. Another important factor, ion friction caused by the interaction of the ionized atmosphere with the neutral flow is also a significant source of wave dissipation. In the presence of Earth's intrinsic magnetic field, GW-induced motions of ions do not coincide with that of neutrals. Ion friction dissipation due to this mismatch influences the attenuation of small-scale GWs during their vertical propagation, determining how high GW harmonics penetrate into the TI. Given the longitudinal variability of the magnetic field geometry, particularly the negative magnetic declination angle in the East and the positive magnetic declination angle in the West CONUS, ion friction dissipation could potentially serve as a contributing factor to the observed longitudinal asymmetry.

Medvedev et al. (2017) derived the vertical damping rate of GW harmonics that accounts for the geometry of the magnetic field and arbitrary propagation directions of the waves. We evaluated the relative vertical damping rates for GWs due to ion friction $\left(\beta_{ion}^{j}\right)$ at East and West CONUS based on the expression (Medvedev et al., 2017, Equation 30):

$$\beta_{ion}^{j} = \frac{\nu_{ni} N}{k_h |c_j - \bar{u}|^2} \left(\cos^2 \alpha + \sin^2 \alpha \cos^2 \gamma\right), \quad (1)$$

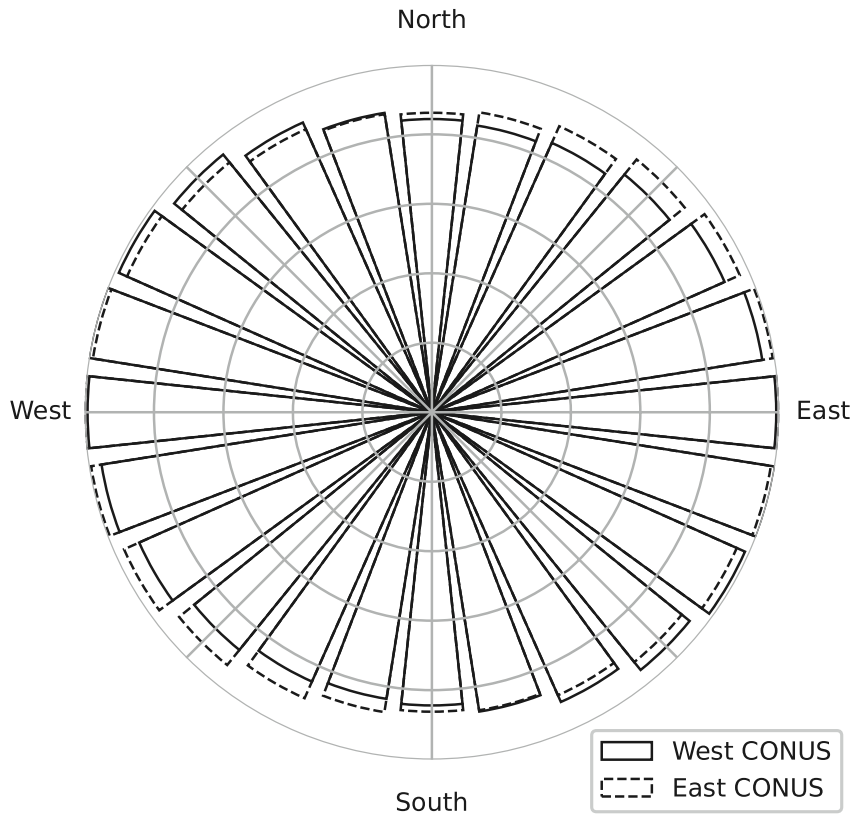

Figure 15. The comparison of the ion friction dissipation of gravity waves propagating at 24 equally spaced geographic directions at the West CONUS (solid line) and at the East CONUS (dashed line) normalized to the maximum dissipation. The outer circle represents maximum dissipation.

where ν_{ni} is the effective collision frequency of neutrals with ions, N is the buoyancy frequency, k_h is the horizontal wave number, and $|c_j - \bar{u}|$ is the speed of wave propagation relative to the zonal wind, or the intrinsic horizontal phase speed. Angle α represents the azimuth of the GW propagation counted counterclockwise from the direction to the geomagnetic east, and γ is the angle between the local vertical and the unit vector in the direction of the magnetic field. The term $\cos^2\gamma$ is approximated as follows (Medvedev et al., 2017, Equation 31):

$$\cos^2\gamma \equiv \frac{B_z^2}{|\mathbf{B}|^2} = \frac{4\sin^2\phi}{1+3\sin^2\phi}, \tag{2}$$

where $\mathbf{B}$ is the magnetic field vector, B_z is its vertical component and ϕ is the geomagnetic latitude. Damping of gravity waves via ion-neutral collisional momentum transfer is an important dissipation processes besides molecular viscosity and nonlinear wave-wave interactions (Yiğit et al., 2008).

According to the International Geomagnetic Reference Field (Alken et al., 2021), the coordinates representing the East and West CONUS in our study have magnetic latitude of 51.31°N and 48.38°N along with magnetic declination of −2.25° and +13.67° at 150 km altitude, respectively. These values are employed to ascertain the geometry of the magnetic field (α and γ) for 24 distinct azimuth directions of gravity wave propagation, each equally spaced by 15°. The parameters associated with wave harmonics (k_h and $|c_j - \bar{u}|$) and background T-I state (N and ν_{ni}) were kept constant, focusing solely on the magnetic field geometry. The results, normalized by the maximum ion friction damping (called form factor), are presented in Figure 15.

Based on Figure 15, gravity waves with zonally aligned azimuths experience higher ion friction compared to the meridionally aligned azimuths in both the East and West CONUS. Notably, there is an obvious longitudinal asymmetry around northeast-southwest (NE–SW) aligned azimuths with the East CONUS experiencing higher

(β_{ion}^{j}). This suggests that GWs propagating along the NE–SW direction attain greater altitudes over the West CONUS, thereby contributing to the observed disturbances in dTEC. While small-scale GWs are not included in our simulations, Figure 12 confirms that the oscillatory positive flare response of the upward winds reaches higher altitudes over the West CONUS, whereas the positive flare response is smooth and gradually diminishes over the East CONUS, as elucidated in Section 3.2. Thus, we can anticipate that the asymmetry in the simulated vertical winds is even more pronounced in reality. These findings indicate a connection between GWs and the longitudinal asymmetry, associated with the geomagnetic influence on ion friction damping of GWs.

4. Summary and Conclusions

We have investigated TEC variability through CONUS during an X1.3 class solar flare. The data is filtered and binned into 2D maps for Continental United States (CONUS). Spectral content and temporal variation of two subregions, namely the East and the West CONUS are analyzed. Their comparison revealed longitudinal asymmetry in ionospheric solar flare response. Although the synchronized global responses were similar in the first ∼100 min after the solar flare, the mean spectral power in the West CONUS reached more than double that in the East CONUS during the following ∼5 hr. There are also discrepancies in the propagation direction of the post-flare disturbances in the East and West CONUS. Local time differences cause the solar terminator-triggered TIDs to emerge coinciding with the solar flare onset in the West CONUS, which are then modified by the flare impacts both in magnitude and wavelength. The meridional propagation of these disturbances in the West CONUS is equatorward; however, there is ambiguity in the zonal propagation, with both eastward and westward propagation. In contrast, the East CONUS, which is relatively quiet after the flare onset, reveals poleward-propagating post-flare disturbances, indicating the role of equatorial electrodynamics. We conducted general circulation model simulations to further examine the longitudinal variability and the relative contributions of the solar flare and the IMF B_z variations on the East–West asymmetry. Results indicate that the southward turning of the IMF had a greater influence on T-I dynamics compared to the solar flare after the first ∼100 min following the solar flare, while their nonlinear interaction introduced complex variations. Simulation results further suggest that the East–West asymmetry results from a combination of local time differences and opposite magnetic declination at the East and West CONUS. An additional analysis based on the gravity wave damping reveals the contribution of T-I couplings to the longitudinal response. The primary findings are as follows:

1. The West CONUS is more variable than the East in terms of dTEC oscillations during the morning hours. The mean spectral power for 4–32 min periods in the pre-flare period is 29%–40% stronger in the West CONUS.
2. The solar flare introduces globally synchronized dTEC oscillations. The mean spectral powers in the East and West CONUS are the same following the first ∼100 minutes after the solar flare.
3. A stronger solar zenith angle dependence for the lower period ionospheric disturbances triggered by the solar flare can be suggested. The mean spectral power for 4–8 min are 24% higher in the East CONUS following the first ∼100 minutes after the solar flare.
4. Enhanced dTEC oscillations are observed after 19:00 UT. Simulation results attribute these variability to the southward turning of the IMF.
5. The East–West asymmetry across the CONUS results from a combination of differences in local time and the Earth's magnetic field geometry.
6. Ion-neutral coupling through ion friction damping of the gravity waves is a potential factor to contribute to the East–West asymmetry.

This study emphasizes the significance of TEC data in ionospheric studies, showcasing its sensitivity to wave-induced disturbances and regional variations. The study's focus on the intricate interplay between the X1.3 solar flare and IMF B_z variations on TEC perturbations across CONUS sheds light on the dynamic responses within the thermosphere-ionosphere system. The impact of the southward turning of the IMF B_z on ionospheric perturbations, along with the substantial contributions of its nonlinear interaction with the solar flare on longitudinal variability, combined with the spatiotemporal variability of GW dissipation, especially due to ion-neutral coupling, underscore the complex dynamics of the ionosphere-thermosphere interaction.

Appendix A: Wavelet Analysis

Continuous wavelet transform $W_p(a, b)$ of a signal corresponding to the time series $X_p(t)$ of pixel p can be expressed as inner products of $X_p(t)$ with a set of dilated (by wavelet scale a) and translated (by localized time parameter b) daughter wavelet function ψ,

$$W_p(a, b) = \frac{1}{\sqrt{a}} \int_{-\infty}^{\infty} X_p(t) \psi\left(\frac{t-b}{a}\right) dt \tag{A1}$$

The complex Morlet wavelet, which is given by

$$\psi(t) = \frac{1}{\sqrt{\pi B}} \exp^{-\frac{t^2}{B}} \exp^{-j2\pi Ct}, \tag{A2}$$

is chosen as the mother wavelet function. B represents the bandwidth and C denotes the central frequency. These two parameters control how well a wavelet can localize events in both time and frequency domains. A wavelet with a narrow bandwidth is adept at capturing fine details in the time domain but may exhibit poor frequency resolution. Conversely, a wavelet with a broader bandwidth provides better frequency information but may compromise time-domain localization (Torrence & Compo, 1998). Considering this inherent trade-off between time and frequency domain resolutions, we carefully selected these constants to achieve a well-balanced resolution for oscillations within the studied period range of 4–32 min.

In order to examine time localized frequency contents in a region composed of N_p pixels, magnitude-squared coherence (MSC) is calculated as:

$$(R(a, b))^2 = \frac{\left|\sum_{p_1, p_2=1}^{N_p} W_{p_1}(a, b) W_{p_2}^*(a, b)\right|^2}{\sum_{p_1=1}^{N_p} |W_{p_1}(a, b)|^2 \sum_{p_2=1}^{N_p} |W_{p_2}(a, b)|^2}, \tag{A3}$$

where $W_{p_1}(a, b), W_{p_2}(a, b)$ are the CWT coefficients of any two pixels in the region. By applying all possible pixel couplings p_1, p_2 in the region of interest, MSC measures similarities of the wavelet coefficients of the input signals. Due to the flexible adjustment of a and b, MSC is able to capture ionospheric disturbances induced by acoustic waves and gravity waves, simultaneously (Yang et al., 2023). In our study, we use b values in the range that covers the length of the dTEC time series of every pixel. The chosen a values range from 2-fold to 5-fold scales, representing disturbance periods spanning 4–32 min.

Data Availability Statement

Line of sight TEC data used in this study (Coster, 2022) is provided by MIT/Haystack Observatory. The modelling results are available at (Sarp et al., 2024).

Acknowledgments
The numerical calculations reported in this paper were fully performed at TUBITAK ULAKBIM, High Performance and Grid Computing Center (TRUBA resources). E.Y. was supported by NASA (Grant 80NSSC22K0016) and NSF (Grant 2330046).

References

Afraimovich, E. L. (2008). First GPS-TEC evidence for the wave structure excited by the solar terminator. *Earth Planets and Space*, *60*(8), 895–900. https://doi.org/10.1186/BF03352843

Afraimovich, E. L., Edemsky, I. K., Voeykov, S. V., Yasukevich, Y. V., & Zhivetiev, I. V. (2010). MHD nature of ionospheric wave packets generated by the solar terminator. *Geomagnetism and Aeronomy*, *50*(1), 79–95. https://doi.org/10.1134/S001679321001010X

Alken, P., Thébault, E., Beggan, C. D., Amit, H., Aubert, J., Baerenzung, J., et al. (2021). International geomagnetic reference field: The thirteenth generation. *Earth Planets and Space*, *73*(1), 49. https://doi.org/10.1186/s40623-020-01288-x

Belcher, S. R. G., Clilverd, M. A., Rodger, C. J., Cook, S., Thomson, N. R., Brundell, J. B., & Raita, T. (2021). Solar flare X-ray impacts on long subionospheric VLF paths. *Space Weather*, *19*(11), e2021SW002820. https://doi.org/10.1029/2021SW002820

Benz, A. O. (2016). Flare observations. *Living Reviews in Solar Physics*, *14*(1), 1–59. https://doi.org/10.1007/s41116-016-0004-3

Briand, C., Doerksen, K., & Deleflie, F. (2021). Solar EUV-enhancement and thermospheric disturbances. *Space Weather*, *19*(12), e2021SW002840. https://doi.org/10.1029/2021SW002840

Bust, G. S., & Mitchell, C. N. (2008). History, current state, and future directions of ionospheric imaging. *Reviews of Geophysics*, *46*(1), RG1003. https://doi.org/10.1029/2006RG000212

Chamberlin, P. C., Eparvier, F. G., Knoer, V., Leise, H., Pankratz, A., Snow, M., et al. (2020). The Flare Irradiance Spectral Model-Version 2 (FISM2). *Space Weather*, *18*(12), e2020SW002588. https://doi.org/10.1029/2020SW002588

Chen, J., Lei, J., Wang, W., Liu, J., Maute, A., Qian, L., et al. (2021). Ionospheric electrodynamic response to solar flares in September 2017. *Journal of Geophysical Research: Space Physics*, *126*(11), e2021JA029745. https://doi.org/10.1029/2021JA029745

Coster, A. (2022). Line of sight TEC data from the cedar madrigal database: 2022-03-30 [Dataset]. *MIT/Haystack Observatory*. Retrieved from https://w3id.org/cedar?experiment_list=experiments4/2022/gps/30mar22&file_list=los_20220330.001.h5

Deng, Y., & Ridley, A. J. (2007). Possible reasons for underestimating joule heating in global models: *E* field variability, spatial resolution, and vertical velocity: Joule heating in global models. *Journal of Geophysical Research*, *112*(A9), A09308. https://doi.org/10.1029/2006JA012006

Foster, M. P., & Evans, A. N. (2008). An evaluation of interpolation techniques for reconstructing ionospheric TEC maps. *IEEE Transactions on Geoscience and Remote Sensing*, *46*(7), 2153–2164. https://doi.org/10.1109/TGRS.2008.916642

Galushko, V. G., Paznukhov, V. V., Yampolski, Y. M., & Foster, J. C. (1998). Incoherent scatter radar observations of AGW/TID events generated by the moving solar terminator. *Annales Geophysicae*, *16*(7), 821–827. https://doi.org/10.1007/s00585-998-0821-3

Goldberg, R. (1966). A theoretical model for the magnetic declination effect in the ionospheric f region (Tech. Rep.).

Habarulema, J. B., Yizengaw, E., Katamzi-Joseph, Z. T., Moldwin, M. B., & Buchert, S. (2018). Storm time global observations of large-scale TIDS from ground-based and in situ satellite measurements. *Journal of Geophysical Research: Space Physics*, *123*(1), 711–724. https://doi.org/10.1002/2017JA024510

Hernández-Pajares, M., Wielgosz, P., Paziewski, J., Krypiak-Gregorczyk, A., Krukowska, M., Stepniak, K., et al. (2017). Direct MSTID mitigation in precise GPS processing. *Radio Science*, *52*(3), 321–337. https://doi.org/10.1002/2016RS006159

Jonah, O. F., Coster, A., Zhang, S., Goncharenko, L., Erickson, P. J., de Paula, E. R., & Kherani, E. A. (2018). TID observations and source analysis during the 2017 memorial day weekend geomagnetic storm over North America. *Journal of Geophysical Research: Space Physics*, *123*(10), 8749–8765. https://doi.org/10.1029/2018JA025367

King, J. H., & Papitashvili, N. E. (2020). Omni 1-min data set. *NASA Space Physics Data Facility*. https://doi.org/10.48322/45BB-8792

Koucká Knížová, P., Laštovička, J., Kouba, D., Mošna, Z., Podolská, K., Potužníková, K., et al. (2021). Ionosphere influenced from lower-lying atmospheric regions. *Front. Astron. Space Sci.*, *8*. https://doi.org/10.3389/fspas.2021.651445

Le, H., Liu, L., Chen, Y., & Wan, W. (2013). Statistical analysis of ionospheric responses to solar flares in the solar cycle 23. *Journal of Geophysical Research: Space Physics*, *118*(1), 576–582. https://doi.org/10.1029/2012JA017934

Li, W., Yue, J., Yang, Y., He, C., Hu, A., & Zhang, K. (2018). Ionospheric and thermospheric responses to the recent strong solar flares on 6 September 2017. *Journal of Geophysical Research: Space Physics*, *123*(10), 8865–8883. https://doi.org/10.1029/2018JA025700

Lilienthal, F., Yiğit, E., Samtleben, N., & Jacobi, C. (2020). Variability of gravity wave effects on the zonal mean circulation and migrating terdiurnal tide as studied with the Middle and Upper Atmosphere Model (MUAM2019) using a nonlinear gravity wave scheme. *Frontiers in Astronomy and Space Sciences*, *7*. https://doi.org/10.3389/fspas.2020.588956

Liu, H., Lühr, H., Watanabe, S., Köhler, W., & Manoj, C. (2007). Contrasting behavior of the thermosphere and ionosphere in response to the 28 October 2003 solar flare. *Journal of Geophysical Research*, *112*(A7), A07305. https://doi.org/10.1029/2007JA012313

Liu, J., Qian, L., Maute, A., Wang, W., Richmond, A. D., Chen, J., et al. (2021). Electrodynamical coupling of the geospace system during solar flares. *Journal of Geophysical Research: Space Physics*, *126*(1), e2020JA028569. https://doi.org/10.1029/2020JA028569

Liu, J. Y., Lin, C. H., Chen, Y. I., Lin, Y. C., Fang, T. W., Chen, C. H., & Hwang, J. J. (2006). Solar flare signatures of the ionospheric GPS total electron content. *Journal of Geophysical Research*, *111*(A5), A05308. https://doi.org/10.1029/2005JA011306

Liu, J. Y., Lin, C. H., Tsai, H. F., & Liou, Y. A. (2004). Ionospheric solar flare effects monitored by the ground-based GPS receivers: Theory and observation. *Journal of Geophysical Research*, *109*(A1), A01307. https://doi.org/10.1029/2003JA009931

Liu, X., Liu, J., Wang, W., Zhang, S.-R., Zhang, K., Lei, J., et al. (2022). Explaining solar flare-induced ionospheric ion upflow at millstone hill (42.6°n). *Journal of Geophysical Research: Space Physics*, *127*(7), e2021JA030185. https://doi.org/10.1029/2021JA030185

Maletckii, B., Yasyukevich, Y., & Vesnin, A. (2020). Wave signatures in total electron content variations: Filtering problems. *Remote Sensing*, *12*(8), 1340. https://doi.org/10.3390/rs12081340

Manju, G., Pant, T. K., Devasia, C. V., Ravindran, S., & Sridharan, R. (2009). Electrodynamical response of the Indian low-mid latitude ionosphere to the very large solar flare of 28 October 2003: A case study. *Annales Geophysicae*, *27*(10), 3853–3860. https://doi.org/10.5194/angeo-27-3853-2009

Mannucci, A. J., Wilson, B. D., Yuan, D. N., Ho, C. H., Lindqwister, U. J., & Runge, T. F. (1998). A global mapping technique for GPS-derived ionospheric total electron content measurements. *Radio Science*, *33*(3), 565–582. https://doi.org/10.1029/97RS02707

Marqué, C., Klein, K.-L., Monstein, C., Opgenoorth, H., Pulkkinen, A., Buchert, S., et al. (2018). Solar radio emission as a disturbance of aeronautical radionavigation. *J. Space Weather Space Clim.*, *8*, A42. https://doi.org/10.1051/swsc/2018029

Medvedev, A. S., Yiğit, E., & Hartogh, P. (2017). Ion friction and quantification of the geomagnetic influence on gravity wave propagation and dissipation in the thermosphere-ionosphere: Gravity wave damping by ion friction. *Journal of Geophysical Research: Space Physics*, *122*(12), 12464–12475. https://doi.org/10.1002/2017JA024785

Mitra, A. P. (1974). *Ionospheric effects of solar flares* (Vol. 46). Springer.

Miyoshi, Y. (2021). Longitudinal variation in the mass density of the thermosphere. In *Upper atmosphere dynamics and energetics* (pp. 217–226). American Geophysical Union (AGU). https://doi.org/10.1002/9781119815631.ch11

Nykiel, G., Zanimonskiy, Y. M., Yampolski, Y. M., & Figurski, M. (2017). Efficient usage of dense GNSS networks in central Europe for the visualization and investigation of ionospheric TEC variations. *Sensors*, *17*(10), 2298. https://doi.org/10.3390/s17102298

Osei-Poku, L., Tang, L., Chen, W., & Mingli, C. (2021). Evaluating Total Electron Content (TEC) detrending techniques in determining ionospheric disturbances during lightning events in a low latitude region. *Remote Sensing*, *13*(23), 4753. https://doi.org/10.3390/rs13234753

Pawlowski, D. J., & Ridley, A. J. (2008). Modeling the thermospheric response to solar flares. *Journal of Geophysical Research*, *113*(A10), A10309. https://doi.org/10.1029/2008JA013182

Qian, L., Burns, A. G., Chamberlin, P. C., & Solomon, S. C. (2010). Flare location on the solar disk: Modeling the thermosphere and ionosphere response. *Journal of Geophysical Research*, *115*(A9), A09311. https://doi.org/10.1029/2009JA015225

Qian, L., Burns, A. G., Liu, H., & Chamberlin, P. C. (2012). Effect of a solar flare on a traveling atmospheric disturbance. *Journal of Geophysical Research*, *117*(A10), A10319. https://doi.org/10.1029/2012JA017806

Qian, L., Wang, W., Burns, A. G., Chamberlin, P. C., Coster, A., Zhang, S.-R., & Solomon, S. C. (2019). Solar flare and geomagnetic storm effects on the thermosphere and ionosphere during 6–11 September 2017. *Journal of Geophysical Research: Space Physics*, *124*(3), 2298–2311. https://doi.org/10.1029/2018JA026175

Qian, L., Wang, W., Burns, A. G., Chamberlin, P. C., & Solomon, S. C. (2020). Responses of the thermosphere and ionosphere system to concurrent solar flares and geomagnetic storms. *Journal of Geophysical Research: Space Physics*, *125*(3), e2019JA027431. https://doi.org/10.1029/2019JA027431

Rideout, W., & Coster, A. (2006). Automated GPS processing for global total electron content data. *GPS Solutions*, *10*(3), 219–228. https://doi.org/10.1007/s10291-006-0029-5

Ridley, A., Deng, Y., & Tóth, G. (2006). The global ionosphere–thermosphere model. *Journal of Atmospheric and Solar-Terrestrial Physics*, *68*(8), 839–864. https://doi.org/10.1016/j.jastp.2006.01.008

Sarp, V., Yiğit, E., & Kilcik, A. (2024). Simulation data for response of the thermosphere-ionosphere system to an x-class solar flare: March 30, 2022 case study [Dataset]. *Zenodo*. https://doi.org/10.5281/zenodo.12256082

Shiokawa, K., & Georgieva, K. (2021). A review of the SCOSTEP's 5-year scientific program VarSITI—Variability of the Sun and its terrestrial impact. *Progress in Earth and Planetary Science*, *8*(1), 21. https://doi.org/10.1186/s40645-021-00410-1

Smith, R. W. (1998). Vertical winds: A tutorial. *Journal of Atmospheric and Solar-Terrestrial Physics*, *60*(14), 1425–1434. https://doi.org/10.1016/S1364-6826(98)00058-3

Sripathi, S., Balachandran, N., Veenadhari, B., Singh, R., & Emperumal, K. (2013). Response of the equatorial and low-latitude ionosphere to an intense x-class solar flare (x7/2b) as observed on 09 august 2011. *Journal of Geophysical Research: Space Physics*, *118*(5), 2648–2659. https://doi.org/10.1002/jgra.50267

Sutton, E. K., Forbes, J. M., Nerem, R. S., & Woods, T. N. (2006). Neutral density response to the solar flares of October and November, 2003. *Geophysical Research Letters*, *33*(22), L22101. https://doi.org/10.1029/2006GL027737

Torr, D., Torr, M., Brinton, H., Brace, L., Spencer, N., Hedin, A., et al. (1979). An experimental and theoretical study of the mean diurnal variation of O^+, NO^+, O_2^+, and N_2^+ ions in the mid-latitude f 1 layer of the ionosphere. *Journal of Geophysical Research*, *84*(A7), 3360–3372. https://doi.org/10.1029/JA084iA07p03360

Torrence, C., & Compo, G. P. (1998). A practical guide to wavelet analysis. *Bulletin of the American Meteorological Society*, *79*(1), 61–78. https://doi.org/10.1175/1520-0477(1998)079⟨0061:APGTWA⟩2.0.CO;2

Tsugawa, T., Otsuka, Y., Coster, A. J., & Saito, A. (2007). Medium-scale traveling ionospheric disturbances detected with dense and wide TEC maps over north America. *Geophysical Research Letters*, *34*(22), L22101. https://doi.org/10.1029/2007GL031663

Vichare, G., Ridley, A., & Yiğit, E. (2012). Quiet-time low latitude ionospheric electrodynamics in the non-hydrostatic global ionosphere–thermosphere model. *Journal of Atmospheric and Solar-Terrestrial Physics*, *80*, 161–172. https://doi.org/10.1016/j.jastp.2012.01.009

Vierinen, J., Coster, A. J., Rideout, W. C., Erickson, P. J., & Norberg, J. (2016). Statistical framework for estimating GNSS bias. *Atmospheric Measurement Techniques*, *9*(3), 1303–1312. https://doi.org/10.5194/amt-9-1303-2016

Ward, W., Seppälä, A., Yiğit, E., Nakamura, T., Stolle, C., Laštovička, J., et al. (2021). Role of the Sun and the Middle Atmosphere/Thermosphere/Ionosphere in Climate (ROSMIC): A retrospective and prospective view. *Progress in Earth and Planetary Science*, *8*(1), 47. https://doi.org/10.1186/s40645-021-00433-8

Weimer, D. R. (2005). Improved ionospheric electrodynamic models and application to calculating joule heating rates. *Journal of Geophysical Research*, *110*(A5), A05306. https://doi.org/10.1029/2004JA010884

Wu, C., Ridley, A. J., DeJong, A. D., & Paxton, L. J. (2021). FTA: A feature tracking empirical model of auroral precipitation. *Space Weather*, *19*(5), e2020SW002629. https://doi.org/10.1029/2020SW002629

Yang, Y.-M., Komanduru, A., & Garrison, J. (2023). Detection of atmospheric-ionospheric disturbances in TEC time series from large GNSS networks using wavelet coherence. *Ieee Journal of Selected Topics in Applied Earth Observations and Remote Sensing*, *16*, 1–26. https://doi.org/10.1109/JSTARS.2023.3276346

Yiğit, E., Aylward, A. D., & Medvedev, A. S. (2008). Parameterization of the effects of vertically propagating gravity waves for thermosphere general circulation models: Sensitivity study. *Journal of Geophysical Research*, *113*(D19), D19106. https://doi.org/10.1029/2008JD010135

Yiğit, E., Frey, H. U., Moldwin, M. B., Immel, T. J., & Ridley, A. J. (2016a). Hemispheric differences in the response of the upper atmosphere to the august 2011 geomagnetic storm: A simulation study. *Journal of Atmospheric and Solar-Terrestrial Physics*, *141*, 13–26. https://doi.org/10.1016/j.jastp.2015.10.002

Yiğit, E., Koucká Knížová, P., Georgieva, K., & Ward, W. (2016b). A review of vertical coupling in the Atmosphere–Ionosphere system: Effects of waves, sudden stratospheric warmings, space weather, and of solar activity. *Journal of Atmospheric and Solar-Terrestrial Physics*, *141*, 1–12. https://doi.org/10.1016/j.jastp.2016.02.011

Yiğit, E., & Medvedev, A. S. (2010). Internal gravity waves in the thermosphere during low and high solar activity: Simulation study. *Journal of Geophysical Research*, *115*(A8), A00G02. https://doi.org/10.1029/2009JA015106

Yiğit, E., Medvedev, A. S., & Ern, M. (2021). Effects of latitude-dependent gravity wave source variations on the middle and upper atmosphere. *Front. Astron. Space Sci.*, *7*, 614018. https://doi.org/10.3389/fspas.2020.614018

Yiğit, E., & Ridley, A. J. (2011a). Effects of high-latitude thermosphere heating at various scale sizes simulated by a nonhydrostatic global thermosphere–ionosphere model. *Journal of Atmospheric and Solar-Terrestrial Physics*, *73*(5–6), 592–600. https://doi.org/10.1016/j.jastp.2010.12.003

Yiğit, E., & Ridley, A. J. (2011b). Role of variability in determining the vertical wind speeds and structure. *Journal of Geophysical Research*, *116*(A12), A12305. https://doi.org/10.1029/2011JA016714

Yizengaw, E. (2021). Ionospheric dynamics and their strong longitudinal dependences. In *Ionosphere dynamics and applications* (pp. 401–419). American Geophysical Union (AGU). https://doi.org/10.1002/9781119815617.ch17

Zhang, K., Liu, J., Wang, W., & Wang, H. (2019a). The effects of imf bz periodic oscillations on thermospheric meridional winds. *Journal of Geophysical Research: Space Physics*, *124*(7), 5800–5815. https://doi.org/10.1029/2019JA026527

Zhang, R., Liu, L., Le, H., & Chen, Y. (2017a). Equatorial ionospheric electrodynamics during solar flares. *Geophysical Research Letters*, *44*(10), 4558–4565. https://doi.org/10.1002/2017GL073238

Zhang, S.-R. (2021). Ionosphere and thermosphere coupling at mid- and subauroral latitudes. In *Ionosphere dynamics and applications* (pp. 339–368). American Geophysical Union (AGU). https://doi.org/10.1002/9781119815617.ch15

Zhang, S.-R., Coster, A. J., Erickson, P. J., Goncharenko, L. P., Rideout, W., & Vierinen, J. (2019b). Traveling ionospheric disturbances and ionospheric perturbations associated with solar flares in September 2017. *Journal of Geophysical Research: Space Physics*, *124*(7), 5894–5917. https://doi.org/10.1029/2019JA026585

Zhang, S.-R., Erickson, P. J., Gasque, L. C., Aa, E., Rideout, W., Vierinen, J., et al. (2021). Electrified postsunrise ionospheric perturbations at millstone hill. *Geophysical Research Letters*, *48*(18), e2021GL095151. https://doi.org/10.1029/2021GL095151

Zhang, S.-R., Erickson, P. J., Goncharenko, L. P., Coster, A. J., Rideout, W., & Vierinen, J. (2017b). Ionospheric bow waves and perturbations induced by the 21 august 2017 solar eclipse. *Geophysical Research Letters*, *44*(24), 12067–12073. https://doi.org/10.1002/2017GL076054

Zhang, S.-R., Foster, J. C., Coster, A. J., & Erickson, P. J. (2011). East-west coast differences in total electron content over the continental us. *Geophysical Research Letters*, *38*(19), L19101. https://doi.org/10.1029/2011GL049116

Zhang, S.-R., Nishimura, Y., Vierinen, J., Lyons, L. R., Knipp, D. J., Gustavsson, B. J., et al. (2023). Simultaneous global ionospheric disturbances associated with penetration electric fields during intense and minor solar and geomagnetic disturbances. *Geophysical Research Letters*, *50*(19), e2023GL104250. https://doi.org/10.1029/2023GL104250

Zhao, B., Wang, M., Wang, Y., Ren, Z., Yue, X., Zhu, J., et al. (2013). East-west differences in f-region electron density at midlatitude: Evidence from the far east region. *Journal of Geophysical Research: Space Physics*, *118*(1), 542–553. https://doi.org/10.1029/2012JA018235

Zhong, J., Lei, J., Dou, X., & Yue, X. (2015). Assessment of vertical TEC mapping functions for space-based GNSS observations. *GPS Solutions*, *20*(3), 353–362. https://doi.org/10.1007/s10291-015-0444-6